Amphipathic Helices Enable Fatty Acid Uptake and Activation by Human FATP2 at ER Contact Sites

Carol Robinson
carol.robinson@chem.ox.ac.uk

University of Oxford https://orcid.org/0000-0001-7829-5505

Haigang Song
University of Oxford https://orcid.org/0000-0002-7568-0544

Rei Matsuoka
OMass Therapeutics

Florencia Klein Rocha
University of Oxford

Jack Bennett
University of Oxford

Tarick El-Baba
University of oxford

Sean Burnap
University of Oxford

Siyuan Song
University of oxford

Carla Kirschbaum
University of Oxford https://orcid.org/0000-0003-3192-0785

Sophie Lawrence
University of oxford https://orcid.org/0009-0005-6652-4792

Lothar Schermelleh
University of Oxford https://orcid.org/0000-0002-1612-9699

Syma Khalid
University of Oxford https://orcid.org/0000-0002-3694-5044

katharina Duerr
University of oxford

Article

Keywords:

Posted Date: March 27th, 2026

DOI: https://doi.org/10.21203/rs.3.rs-8895167/v1

Additional Declarations: Yes there is potential Competing Interest. C.V.R. is a cofounder of and scientific advisor at OMass Therapeutics. The other authors declare no competing interests.

Amphipathic Helices Enable Fatty Acid Uptake and Activation by Human FATP2 at ER Contact Sites

Haigang Song,[1,2]* Rei Matsuoka,[3] Florencia Klein Rocha,[4] Jack L. Bennett,[1,2] Tarick J. El-Baba,[1,2] Sean A. Burnap,[1,4] Siyuan Song, [1,2] Carla Kirschbaum,[1,2] Sophie A. S. Lawrence,[1,2] Lothar Schermelleh,[4] Syma Khalid,[4]
Katharina Duerr,[1,3] Carol V. Robinson[1,2]*

1. Kavli Institute for Nanoscience Discovery, Dorothy Crowfoot Hodgkin Building, University of Oxford OX1 3QU, United Kingdom.

2. Department of Chemistry, University of Oxford, OX1 3TA, United Kingdom.

3. OMass Therapeutics, Oxford, OX4 2GX, United Kingdom.

4. Department of Biochemistry, University of Oxford, OX1 3QU, United Kingdom.

*Correspondence to: haigang.song@chem.ox.ac.uk, carol.robinson@chem.ox.ac.uk

Abstract (163 words)

Fatty acid transport proteins (FATPs) couple fatty acid uptake to metabolic activation; a process frequently dysregulated in metabolic disease and cancer. However, the structural basis of the coupling has remained unclear. Here we combine native mass spectrometry and cryo-EM to capture fatty acyl-adenylate intermediates and determine the first high-resolution structures of a FATP family member, FATP2. The structures reveal two functionally separable modules: an amphipathic helix module enabling membrane-dependent uptake and a catalytic activation module mediating metabolic trapping. Structure-guided mutagenesis demonstrates that the helices are essential for fatty acid uptake, whereas a catalytically inactive splice variant (FATP2b) uncouples membrane-dependent uptake from activation. Molecular dynamics simulations indicate that the two amphipathic helices induce lipid-packing defects and membrane thinning. Consistently, super-resolution live-cell imaging and co-immunoprecipitation show that FATP2 localizes to the endoplasmic reticulum and preferentially associates with ER–organelle contact sites. Together our data establish FATP2 as a prototype for membrane geometry-coupled metabolic enzymes and provide a structural framework for the development of FATP-targeted therapeutics.

Introduction.

Fatty acids (FAs) are essential energy substrates that also serve as precursors for triglycerides and phospholipids, and function in hormone production, second-messenger signalling, and protein post-translational lipidation. Dysregulation of fatty acid metabolism underlies numerous diseases including type 2 diabetes mellitus[1], obesity[2], non-alcoholic fatty liver disease[3], and cancer[4].

In mammalian cells, long-chain fatty acids (LCFAs, C12–C20) and very-long-chain fatty acids (VLCFAs, >C20) arise from *de novo* synthesis via ER-mediated elongation and desaturation[5], dietary uptake, and peroxisomal β-oxidation[6]. Extracellular uptake of LCFAs is thought to proceed through several sequential steps: i) delivery to the plasma membrane (PM); ii) insertion into the outer leaflet; iii) trans-bilayer flip-flop; and iv) extraction from the inner leaflet[7]. Whereas short- and medium-chain FAs cross membranes rapidly by passive flip-flop[8], (V)LCFAs typically require protein-facilitated uptake[9]. Several protein systems mediate this process, including the cell surface scavenger receptor CD36[10], PM-associated fatty acid binding proteins ($FABP_{pm}$)[11], and the FATPs. Fatty acid transporter proteins (FATPs, SLC27A1–6) constitute a family of integral membrane proteins with tissue-specific expression[12] that generally couple fatty acid uptake to acyl-CoA synthetase activity (**Fig. 1a**), thereby metabolically trapping incoming substrate[6,13,14]. Dysregulation of FATPs contributes to non-alcoholic fatty liver disease[15,16], cancer progression[9], and kidney disease[10], and pathogenic mutations in FATP4 cause ichthyosis prematurity syndrome[11].

The subcellular localization of FATPs has remained elusive, with individual family members reported at the PM[17,18,19], ER[20-22], peroxisome[19], mitochondria[23], or in lipid droplets[24]. Notably, several FATPs have been proposed to form functional complexes at organelle interfaces, including FATP1–DGAT2 in ER–lipid droplet interface[24] and FATP4–PLIN5 in mitochondria-lipid droplet interface[25]. More recently, membrane contact sites between caveolae and the ER have been implicated in FATP1-mediated fatty acid uptake[26]. These observations prompted us to consider whether FATPs might not function within a single cellular compartment but instead operate within distinct membrane subdomains or at inter-organelle interfaces, where local membrane environments could influence fatty acid uptake and activation.

To uncover the effects of membrane environments on FATP function, here we elucidate how FATP2 engages and activates membrane-embedded fatty acids at specific membrane subdomains. Guided by native mass spectrometry (nMS), we report the first high-resolution cryo-EM structures of a FATP family member. These structures allow us to visualize fatty acyl-adenylate intermediates, $PI(4,5)P_2$ binding enable us to deduce the mechanism of inhibition for a synthetic inhibitor, Lipofermata. Super-resolution live-cell imaging and co-immunoprecipitation indicate that FATP2 is an ER-resident protein and preferentially associates with ER–organelle contact sites. Our structure and molecular dynamics (MD) simulations also reveal that FATP2 utilises two amphipathic helices to engage the membrane and promote lipid-packing defects, facilitating fatty acid access through a membrane-interfacial tunnel. Mutations in the amphipathic helices, or $PI(4,5)P_2$ depletion, impair FATP2-mediated (V)LCFA uptake. Overall, our results provide a structural framework for membrane geometry-dependent regulation and pharmacological targeting of this transporter family.

Results

FATP2 mediates uptake and catalyses fatty acyl-CoA formation

We first evaluated FATP2-mediated fatty acid uptake using an established fluorescence-based assay[27,28]. We compared HEK293T and HeLa cells overexpressing full-length FATP2. Relative to empty vector controls, 2.5-fold and 1.3-fold increases in BODIPY FL C_{16} uptake were observed respectively for HEK293T and HeLa cells (**Fig. 1b, Extended Data Fig. 1**). Given the more pronounced response, HEK293T cells were selected for subsequent assays and is consistent with previous reports[9,10,14,27] that FATP2 mediates fatty acid uptake.

We next generated a stable HEK293S GNTI$^-$ TetR cell line[29] to overexpress full-length C-terminal FLAG-tagged FATP2 enabling purification to homogeneity (**Supplementary Fig. 1**). A mild detergent solution, containing *n*-dodecyl-β-D-maltoside (DDM) and cholesteryl hemisuccinate (CHS), yielded a monodisperse species as assessed by size-exclusion chromatography (**Supplementary Fig. 6**). We then recorded a native mass spectrum (nMS) of purified FATP2 in positive ion mode. The mass spectrum revealed two charge state distributions between *m*/*z* 3,000 and 6,000, corresponding to monomeric FATP2 (71,309 Da, theoretical 71,307 Da) and dimeric FATP2 (142,612 Da, theoretical 142,615 Da) (**Fig. 1c**). Notably, expansion of the nMS spectrum of FATP2 monomer revealed three satellite peaks with mass shifts of +238, +586, and +614 Da relative to the unmodified protein (**Fig. 1c**). The +238 Da adduct (~21% intensity of the unmodified protein) was also observed in the nMS spectrum collected in negative ion mode (**Supplementary Fig. 9**) and was assigned to a single palmitoyl addition (**Fig. 1c**). The +586 and +614 Da adducts could not be assigned to canonical lipids or known post-translational modifications.

To identify these unknown species, we acquired nMS spectra of FATP2 on an Orbitrap Eclipse in negative ion mode. Under high in-source activation conditions, we observed deprotonated ions at *m*/*z* 584.2807 and 612.3109 ($[M-H]^-$) at low *m*/*z* regions, consistent with the unknown adducts (**Fig. 1d**). Fragmentation of these two ions using higher-energy collisional dissociation yielded a fragment ion at *m*/*z* 346.0547 (**Fig. 1d**). We assigned this species as deprotonated adenosine monophosphate (mass error = −1.7 ppm)[30]. Based on these results and the known function of FATP2, we assigned the adducts to palmitoyl adenylate (mass error = −7.3 ppm) and stearoyl adenylate (mass error = −8.7 ppm) (**Fig. 1d**). These two adenylate intermediates represent the first steps of adenylate-formation which are then available to react with coenzyme A (CoA) to produce acyl-CoA[31,32]. To test whether FATP2 catalyses the second step, we incubated purified FATP2 separately with ATP or free CoA and recorded native mass spectra. The + 586 Da palmitoyl adenylate and +614 Da stearoyl adenylate adducts disappeared only upon addition of free CoA (**Extended Data Fig. 2**), demonstrating that purified FATP2 is enzymatically active.

We next examined the ensemble of fatty acids that co-purified with FATP2 using established LC-MS lipidomics[33]. Our analyses revealed selective enrichment of several (V)LCFAs, including C20:0, C20:1, C20:4, C22:4, C22:6, and C24:0 (**Extended Data Fig. 3a**), with arachidonic acid (C20:4) as the most enriched (12-fold) compared to whole crude membrane. We later probed FATP2's substrate specificity by incubating the purified protein with a panel of saturated and unsaturated (V)LCFAs and free CoA. We monitored product formation by native MS and observed the highest intensity products upon incubation with C20:4 and C24:1 (mass shifts of +1,052 Da (error = 2 Da) and +1,116 Da (error = 0 Da) respectively) (**Extended Data Fig. 3b**). These observations are consistent with the known preference of FATP2 for unsaturated fatty acids[34]. We therefore performed an *in vitro* activity assay in buffer containing DDM using arachidonic acid as a substrate and determined steady-state kinetic parameters by fitting to a substrate inhibition Michaelis-Menten equation: $k_{cat} = 0.096 \pm 0.017$ min^{-1}, $K_M = 76.7 \pm 5.9$ μM and $K_I = 58.9 \pm 6.4$ μM (**Extended Data Fig. 3c**). The substrate inhibition suggests a possible alternative fatty acid binding mode under high substrate concentration conditions (**Supplementary Fig. 10**).

Cryo-EM structure of human FATP2

Given that our nMS demonstrated that FATP2 forms ~142 kDa dimers in detergents, a suitable size for single-particle cryo-EM, we used these conditions to determine the structure of full-length FATP2 in DDM/CHS micelles at 3.8 Å resolution (**Fig. 1e, Supplementary Fig. 7**). The map revealed an unusual antiparallel homodimer formed by interactions between the N-terminal helices (**Extended Data Fig. 4a-b**). Since soluble catalytic domains sit in the cytoplasm *in vivo*, this arrangement likely results from detergent solubilization. Considering one protomer, we successfully traced its full sequence (residues 1–620). We divided FATP2 into three regions: an N-terminal anchoring helix (residues 1–23), a large central domain (residues 25–480), and a C-terminal domain (residues 481–620) (**Fig. 1f**). The central and C-terminal domains adopt the canonical adenylate-formation protein fold, and superimpose with the medium-chain acyl-CoA synthetase ACSM2A from human (PDB 2WD9) with an RMSD of 2.4 Å over 392 Cα atoms[35]. The C-terminal domain adopts a compact α/β fold with a β-hairpin and five-stranded β-sheet flanked by four helices (**Fig. 1f**). Orientations of Proteins in Membranes analysis[36] predicted that the anchoring helix tilts ~18° relative to the bilayer. In addition to the conserved ANL-fold, FATP2 contains two amphipathic helices (APHs) unique to this transporter: APH1 (α2, residues 25–49) and APH2 (α17, residues 386–391) (**Fig. 1f**).

Structural determinants of fatty acid entry

Close inspection of the EM map revealed additional density extending from Cys22. Using information from nMS we modelled a covalently attached palmitoyl group (**Fig 1f**). The palmitoyl chain is partially embedded in the membrane, likely anchoring FATP2 within the bilayer. We also observed a continuous density (**Fig. 2a**) extending from APH1 and APH2 into a ~28 Å hydrophobic tunnel at the interface of the central and C-terminal domains (**Fig. 2b**). Guided by nMS results, we modelled stearoyl adenylate (C18:0–AMP) into this density in two alternate conformations: a linear *trans* configuration and a kinked geometry with an ω-shaped hook near the terminal acyl chain (**Fig. 2a, c**). The latter conformation could accommodate *cis* double bonds near Δ8/Δ11/Δ14, providing a structural rationale for the enzyme's preference for arachidonic acid (20:4 *n*-6; Δ5,8,11,14) (**Extended Data Fig. 3a, b**).

Comparing the other acyl-CoA synthetases in the FATP family we found that FATP2 closely resembles the other five family members with conserved catalytic motifs and adenylation active sites (**Supplementary Fig. 12**). In the adenylate-bound structure, AMP sits between the central and C-terminal domains: adenine stacks against F477 and Y362 and hydrogen bonds with N339 and the backbone of F361; the ribose hydroxyl groups contact D465; and the phosphate group interacts with H268 and forms a salt bridge with K572 (**Supplementary Fig. 11**). K572 resides in the conserved A10 motif, a signature sequence element of adenylate-formation enzymes that coordinates ATP and configures the active site[31,32]. The fatty acid carbonyl forms hydrogen bonds with H268, a residue essential for substrate activation across FATPs and long-chain acyl-CoA synthetases; notably, mutation of the equivalent histidine in FATP5 (H338) is pathogenic and disrupts bile acid conjugation causing neonatal liver disease[37].

The tunnel entrance is formed by residues from both APHs and an adjacent loop (V36, A37, V39, G40, V43, I391, I392, T433, L432) (**Fig. 2c**). The ~28 Å tunnel interior is lined by hydrophobic residues including Y32, L248, F250, V251, A270, L273, L274, F361, and M372 **(Fig. 2c)**. In the kinked conformation of the bound acyl chain, additional contacts are made with Y32, V36, L248, V251, F361, and M372 (**Fig. 2c**). The tunnel opens towards the cytosolic leaflet, consistent with the structural orientation of the APHs, suggesting that membrane-embedded fatty acids enter the active site through this interfacial tunnel.

To evaluate the functional importance of this tunnel, we introduced bulky tryptophan substitutions at residues lining the tunnel entrance (V36, A37, V39, I391, I392, and L432), and within the tunnel interior (L248) (**Fig. 2c)**. Each variant was transiently expressed in HEK293T cells, and fatty acid uptake activity was measured and normalized to protein expression determined by western blot (**Fig. 2d, Extended Data Fig. 5, Supplementary Fig. 3**). Most single substitutions markedly impaired uptake, with the strongest effect observed for V36W, V37W, and L248W and the weakest for I392W (**Fig. 2d, Extended Data Fig. 5**). Double and triple substitutions (I391W/I392W and I391W/I392W/L432W) produced even greater impairments. Given that tryptophan introduces considerable steric bulk, these effects are consistent with partial narrowing or distortion of the tunnel, thereby restricting the lateral access of fatty acids to the active site. Together, these results support the functional importance of the identified tunnel and highlight how bulky residues inhibit fatty acid entry.

Mechanism for FATP2 inhibition by Lipofermata

We next considered the impact of the inhibitor Lipofermata (**Fig. 2e**), which has been reported to inhibit FATP2-mediated LCFA uptake without affecting activation[27]. First, we evaluated the effect of Lipofermata on fatty acid uptake in HEK293T cells overexpressing FAPT2. We observed a dose-dependent inhibition, with an IC_{50} of 4.0 µM (**Extended Data Fig. 6a)**. To address whether FATP2 enzymatic activity was also affected, we quenched the *in vitro* reaction mixture in the presence or absence of 100 µM Lipofermata and detected production of C20:4–CoA by MS. Notably, C20:4–CoA production was reduced approximately 2-fold (**Fig. 2f, Extended Data Fig. 6b**), indicating Lipofermata not only inhibits access but also suppresses synthetase activity, contrary to an earlier report[27].

To determine the structural basis of this inhibition, we incubated purified FATP2 with high concentrations of Lipofermata and solved the structure of the complex at 3.9 Å resolution (**Supplementary Fig. 8**). Compared with the adenylate-bound complex, the overall structure of the N-terminal helix and central domain could be clearly resolved and remained largely unchanged. The C-terminal domain, however, was less resolved, suggesting increased flexibility upon loss of the adenylate intermediate. Moreover, we observed additional density at the AMP-binding site accompanied by loss of density for the fatty acid chain (**Fig. 2g**). This density was modelled as the *R*-enantiomer of Lipofermata. The compound is stabilized by multiple interactions: hydrophobic contacts between its phenyl ring and A364/R480, indoline ring with N339 and G340; π–π stacking between the indoline moiety and F477, (**Fig. 2g**). N339, D465, and R480, previously predicted to participate in Lipofermata binding[38], are positioned nearby. This Lipofermata structure therefore confirms our mechanistic interpretation that Lipofermata occupies the AMP-binding site and suppresses synthetase activity.

Acyl-CoA synthetase activity is not essential for *in vivo* fatty acid uptake

To explore the mechanism coupling uptake and activation further, we employed FATP2b (Δ230–282), a natural splice variant of FATP2 lacking the A3 and A4 motifs required for ATP binding within the adenylate-forming family of enzymes[32]. This variant retains the anchoring helix, the two APHs (**Fig. 3a, Supplementary Fig. 12**), and a partial substrate tunnel according to the Alpha-Fold structure of FATP2b (**Extended Data Fig. 7a–b**). To investigate its activity, we transiently expressed FATP2b in HEK293T cells and monitored the uptake of BODIPY FL C_{16}. FATP2b increased uptake when compared to empty vector controls (**Extended Data Fig. 7c**), and when normalized for expression, showed uptake activity comparable to wild-type FATP2 (**Fig. 3b, Extended Data Fig. 7d, Supplementary Fig. 5**).

To directly assess the catalytic activity of FATP2b, we purified the protein similarly to FATP2 (**Supplementary Fig. 2**). Incubation with arachidonic acid, ATP, and free CoA, followed by acid quenching and MS analysis, revealed no detectable C20:4–CoA product at low mass ranges (m/z = 500–2,000), even following prolonged reaction times (1 h) at room temperature. By contrast, appreciable quantities of C20:4–CoA were detected for the wild-type protein (**Fig. 3c**). These results agree with a previous report that showed that FATP2b retains uptake activity despite being catalytically inactive[34]. Together, these results indicate that although acyl-CoA synthetase activity enhances uptake efficiency (**Fig 2f**, **Extended Fig. 6**), it is not essential for fatty acid uptake.

Structural and biophysical properties of FATP2 amphipathic helices

To understand how FATP2 accesses membrane-embedded fatty acids, we orientated our FATP2 cryo-EM structure on membrane using Orientations of Proteins in Membranes analysis[36]. This analysis implies that both amphipathic helices are oriented toward the cytosolic leaflet (**Fig. 4a**). The N-terminal segment of APH1 (residues 25–34) is enriched in bulky hydrophobic residues (Y25, F26, F27, I30, Y32, F33, and L34), whereas the C-terminal segment (residues 35–49) contains multiple basic residues (K35, R41, R42, R44, K48, and R49) **(Fig. 4a**, **Extended Data Fig. 8a**). It is therefore likely that the N-terminal segment penetrates into the hydrophobic core of the bilayer, while the C-terminal segment remains positioned near the lipid headgroup interface (**Fig. 4a**). APH2 inserts more shallowly, with Y386 and L387 contacting the hydrophobic core, and K389 and K390 aligning to engage phospholipid headgroups (**Fig. 4a, Extended Data Fig. 8a**). Helical wheel projections of APH1 and APH2 confirm the amphipathic character of both helices, revealing hydrophobic residues clustered on one face and charged residues on the opposite (**Fig. 4a, Extended Data Fig. 8a**). A salt bridge between D29 and R383 implies likely coordinated movement of the two helices (**Fig. 4a**). Together, these two APHs orient the fatty acid entry tunnel toward the cytosolic leaflet, positioning FATP2 to capture membrane-embedded substrates.

The architecture of APH1 with two distinct segments supports a dual mode of membrane interaction. The hydrophobic N-terminal segment could enable a wedge-like insertion into the lipid bilayer, analogous to the Sar1p-mediated membrane insertion[39-41]. The basic C-terminal segment, on the other hand, could form electrostatic interactions with negatively charged lipid headgroups, a process often associated with the induction of membrane curvature, analogous to that observed in epsin[42]. We calculated properties of APH1 across the FATP family (**Fig. 4b**, **Extended Data Fig. 8b**) and compared them with APHs from known amphipathic lipid packing sensors (ALPSs), membrane curvature-inducers, and ER-shaping proteins (**Fig. 4b**). FATP2, together with several other FATPs, occupies a region of parameter space with known curvature-inducing amphipathic helices (**Fig. 4b**, top right quadrant). This region is defined by a high density of bulky hydrophobic residues (overall ~30%) and substantial bending potency (D-factor > 1.33), exceeding that of canonical curvature sensors **(Fig. 4b, Supplementary Fig. 13).** FATPs also exhibit high net charges, comparable to epsin[42,43] and bridging integrator 1 (bin1)[44] **(Fig. 4b, Supplementary Fig. 13)**. It is therefore likely that the APHs in the FATP family couple membrane engagement to local curvature or lipid packing defects[40,41,45-50].

To examine how FATP2 engages and perturbs the membrane, we performed atomistic molecular dynamics simulations of FATP2 in an ER-mimetic lipid bilayer. Consistent with shallow amphipathic helix insertion predicted in Orientations of Proteins in Membranes analysis, FATP2 induces bilayer thinning by ~0.6–0.7 nm and increases lipid acyl-chain tilt by ~10–12° within 1.5 nm of the protein centre, with recovery to bulk membrane values at larger distance (4 nm) (**Fig. 4c**). In addition, analysis of lipid–protein contacts revealed prolonged residence of phosphatidylserine (POPS) near the two amphipathic helices, in accord with electrostatic engagement of anionic lipids (**Extended Data Fig. 9a,b**). Together, these simulations support a model in which FATP2 utilizes amphipathic helices to cause lipid packing defects.

To assess whether FATP2 directly associates with negatively charged lipids, we recorded nMS spectra of FATP2 in the presence of various anionic phospholipids. Incubation with C18:1 phosphatidic acid (PA), phosphatidylserine (PS), phosphatidylinositol 4,5-bisphosphate (PI(4,5)P_2), yielded additional adduct peaks corresponding to FATP2-lipid complexes (**Fig. 4d**), suggesting direct electrostatic interactions between FATP2 and lipids. These data suggest that the polybasic faces of APHs might mediate interactions with anionic lipids. We next examined functional contributions of these basic residues in APH1 to fatty acid uptake by substitution with alanine and quantifying BODIPY FL C_{16} uptake in a cell-based assay. Single basic residue substitutions (R41A, R44A, R50A) significantly reduced uptake (**Fig. 4e, Extended Data Fig. 10, Supplementary Fig. 4**), whereas R42A, K48A, and R49A had a smaller effect. Multiple residue substitutions (R41A/R42A/R44A or K48A/R49A/R50A) also caused significantly reduced, yet non-additive, LCFA uptake activity (**Fig. 4e, Extended Data Fig 10, Supplementary Fig. 4**). These data imply that the polybasic face of APH1 mediates interactions with anionic lipids in the membrane bilayer that are required for efficient LCFA uptake.

FATP2 is associated with ER-PM tethers for fatty acid uptake

Given the proposed role of FATP1-mediated fatty acid uptake at ER contact sites[26], to assess FATP2 localization, we used super-resolution total reflection fluorescence structured illumination microscopy (TIRF-SIM) of U2OS cells co-expressing FATP2-

Halo and eGFP-ESYT2. Extended synaptotagmin-2 (ESYT2) is an ER-anchored lipid transfer protein that tethers the ER-PM contact sites, making it a reliable marker for visualizing these junctions in imaging experiments[51]. We found that ESYT2 exhibited a continuous reticular distribution characteristic of cortical ER (**Fig. 5a–b**), whereas FATP2 was enriched in discrete puncta along ESYT2-positive structures (**Fig. 5a–c**). FATP2 puncta were frequently positioned adjacent to ESYT2-labeled tubules with signals showing partial overlap (**Fig. 5d**). Assessing the coordinated variations in FATP2 and ESYT2 signal intensity along individual tubules, intensity maxima were found to be often offset rather than coincident, as revealed by curvilinear profile plot analyses (**Extended Data Fig. 11**). These observations indicate that FATP2 and ESYT2 occupy closely associated subdomains within the cortical ER network, with FATP2 concentrated in punctate assemblies positioned along ESYT2-marked ER–plasma membrane contact regions.

To define FATP2 interacting proteins at these sites, we performed FLAG-immunoprecipitation followed by quantitative proteomics using FATP2-FLAG as bait in HeLa cells. FATP2 immunoprecipitants were significantly enriched in ER–PM tethering components (e.g., VAPA), and curvature-associated membrane-shaping proteins (e.g., CAV1, REEP5), compared to empty vector controls (**Fig. 5e**). FATP2 also co-purified with proteins implicated in ER contacts with other organelles (**Fig. 5e**), indicating that FATP2 associates with a contact site-enriched ER subdomain. Inspired by these results, we mined a published immunoprecipitation–MS dataset using ESYT1, ESYT2, and VAPB as baits in HepG2 cells[52] and a published proximity-labelling dataset from a BioID map of the HEK293 proteome[53]. We found that FATP2 is consistently enriched in ER contact site-associated compartments defined by established tethering proteins (ESYTs and VAP complexes) and membrane-shaping factors (reticulons, trafficking GTPases, atlastins, and REEP family members) (**Extended Data Fig. 12a–d)**. Notably, many of these proteins promote or stabilize membrane curvature through amphipathic helix insertion, either directly (SAR1B, ARL6IP1)[39,54,55,] or in combination with intramembrane hairpins (REEPs, RTNs, RETRs, atlastins)[47,48,56-59,].

PI(4,5)P_2 is a key organizing lipid of ER–PM junctions, mediating ESYTs tethering[60] and the recruitment of VAP-associated lipid transfer proteins via their pleckstrin homology domains[61,62]. We therefore tested whether PI(4,5)P_2 is required for FATP2 function. Pharmacological depletion of PI(4,5)P_2[63] using the PIP5K1A inhibitor ISA-2011B[64] or the PIP5K1C inhibitor UNC3230[65] markedly reduced FATP2-mediated fatty acid uptake in HEK293T cells (**Fig. 5f**).These results suggest that FATP2 uptake activity depends on PI(4,5)P_2-dependent membrane organization, consistent with a requirement for ER–PM contact site integrity.

Discussion

FATPs have long been recognized for their role in fatty acid uptake and intracellular activation, yet the mechanism underlying these coupled processes has remained unclear. Here, by integrating cryo-EM and nMS with biophysical analysis and cellular imaging, we propose a novel mechanism in which FATP2 employs APHs to engage and perturb local membranes, promoting localization at curved ER membrane contact sites and enabling fatty acid extraction directly from the lipid bilayer. Our data therefore support a curvature-coupled mechanism in which membrane geometry modulates FATP2's function.

The cryo-EM structure of the protein–adenylate complex reveals an adenylate-binding pocket shared with other FATPs and bacterial acyl-CoA synthetases[66]. However, the orientation of the acyl chain points towards the membrane, suggesting a distinct strategy for substrate extraction directly from the bilayer (**Fig. 4a**). A long hydrophobic tunnel connects the cytosolic leaflet to the catalytic centre, enabling fatty acids to enter laterally from the bilayer rather than through a classical transmembrane pore (**Fig. 2b**). This architecture directly couples membrane engagement to catalysis, with distinct but coordinated structural elements mediating each step. The geometry and properties of the long tunnel in FATP2 favour polyunsaturated fatty acids (**Fig. 2a, c**), consistent with previous observations of FATP2-dependent trafficking of *n*-3 fatty acids[34] and its role in arachidonic acid uptake and prostaglandin E2 production in cancer[9].

A central insight of this study is the role of the APHs in coupling membrane geometry to fatty acid uptake. These two APHs are enriched with bulky hydrophobic residues and a high net positive charge (**Fig. 4a**), enabling both wedge-like perturbation of lipid packing and electrostatic interactions with anionic lipid headgroups on the inner leaflet (**Fig. 4c**)[39,42-44]. In this respect, the FATP2 APHs differ from ALPS motifs, which have low net charge and primarily detect pre-existing curvature[45,67]. The lipid packing defects characteristic of membrane thinning and lipid tilting also lower the energetic barrier for both fatty acid insertion and extraction from the lipid bilayer[68]. This curvature-dependent mechanism clarifies the relationship between fatty acid uptake and activation. This mechanism is supported by the splice variant FATP2b which lacks the catalytic adenylation motif yet contains amphipathic helices, retains partial tunnel architecture, and is capable of fatty acid uptake activity (**Fig. 3**). These observations indicate that membrane engagement and curvature-dependent substrate insertion/extraction are primary determinants of uptake in the cell. The acyl-CoA synthetase activity confers metabolic trapping and directionality. In addition to FATP2-mediated adenylation, other cellular acyl-CoA synthetases or lipid-utilizing enzymes may contribute to metabolic trapping and directionality at membrane contact sites. Transport and activation are therefore closely linked but partially separable processes, unified by initial membrane deformation.

The membrane lipid composition and spatial organization identified here are consistent with enrichment of FATP2 at ER–plasma membrane contact sites, where curved ER membranes interface with the plasma membrane (**Fig. 6**). Such environments are optimised for APH insertion, electrostatic interactions, and lipid packing defects, and are increasingly recognized as hubs for lipid exchange and metabolic regulation[69]. FATP2 therefore exemplifies how metabolic enzymes can exploit such membrane geometry and composition to couple fatty acid uptake to activation. Together, our findings position FATP2 as a prototype for curvature-coupled metabolic enzymes, highlighting how membrane physical properties can shape lipid uptake and metabolic activation.

Funding

Research in the C.V.R. laboratory is supported by a Medical Research Council (MRC) (MR/V028839/1) and Wellcome Trust (221795/Z/20/Z) grants.

Acknowledgements

We thank Vasiliki Tsioligka for providing technical assistance with fluorescence-assisted cell sorting at The Don Mason Facility of Flow Cytometry, Sir William Dunn School of Pathology, University of Oxford. The authors gratefully acknowledge Niloufer Irani at the Micron Bioimaging Facility for their support & assistance in this work. The authors would also like to thank Patrik Risteski from Weatherall Institute of Molecular Medicine, University of Oxford, for aiding with imaging data analysis.

Author Contributions

H.S. and C.V.R. designed the study. H.S. designed constructs and generated expression cell lines with assistance from T.J.E. and S.A.S.L.. H.S. performed protein purification and carried out western blotting. R.M. collected the cryo-EM data and built the initial model. H.S. and R.M. performed the ligand fitting, structure refinement and analysis. H.S. collected and analysed nMS and nTDMS with assistance from J.L.B and C.K. H.S. performed mutagenesis and cell-based assay with assistance from S.S. H.S. performed and analysed lipidomics. H.S. performed co-immunoprecipitation and LC-MS analysis with assistance from J.L.B. and S.B. H.S. performed the re-analysis of the published and public co-IP and proximity labelling data. H.S. and L.S. performed the TIRF-SIM imaging and analysis. F.K.R. and S.K. performed the MD simulation. H.S. and C.V.R. wrote the manuscript with assistance from K.D, and input from all authors.

Data Availability

The raw native MS data and lipidomics generated in this study have been deposited in the Figshare database. The proteomics raw data generated in this study have been deposited in the MassIVE database under the accession number p47T5f00fWa5o58n. Atomic coordinates for the model have been deposited to the Protein Data Bank (PDB) under the accession numbers 28KF, and 28KR. The 3D-cryo-EM maps have been deposited in the Electron Microscopy Data Bank (EMDB) under the accession numbers EMD-56574, and EMD-56581. Uncropped Western blots and SDS-Page gels are shown in the Supplementary Information.

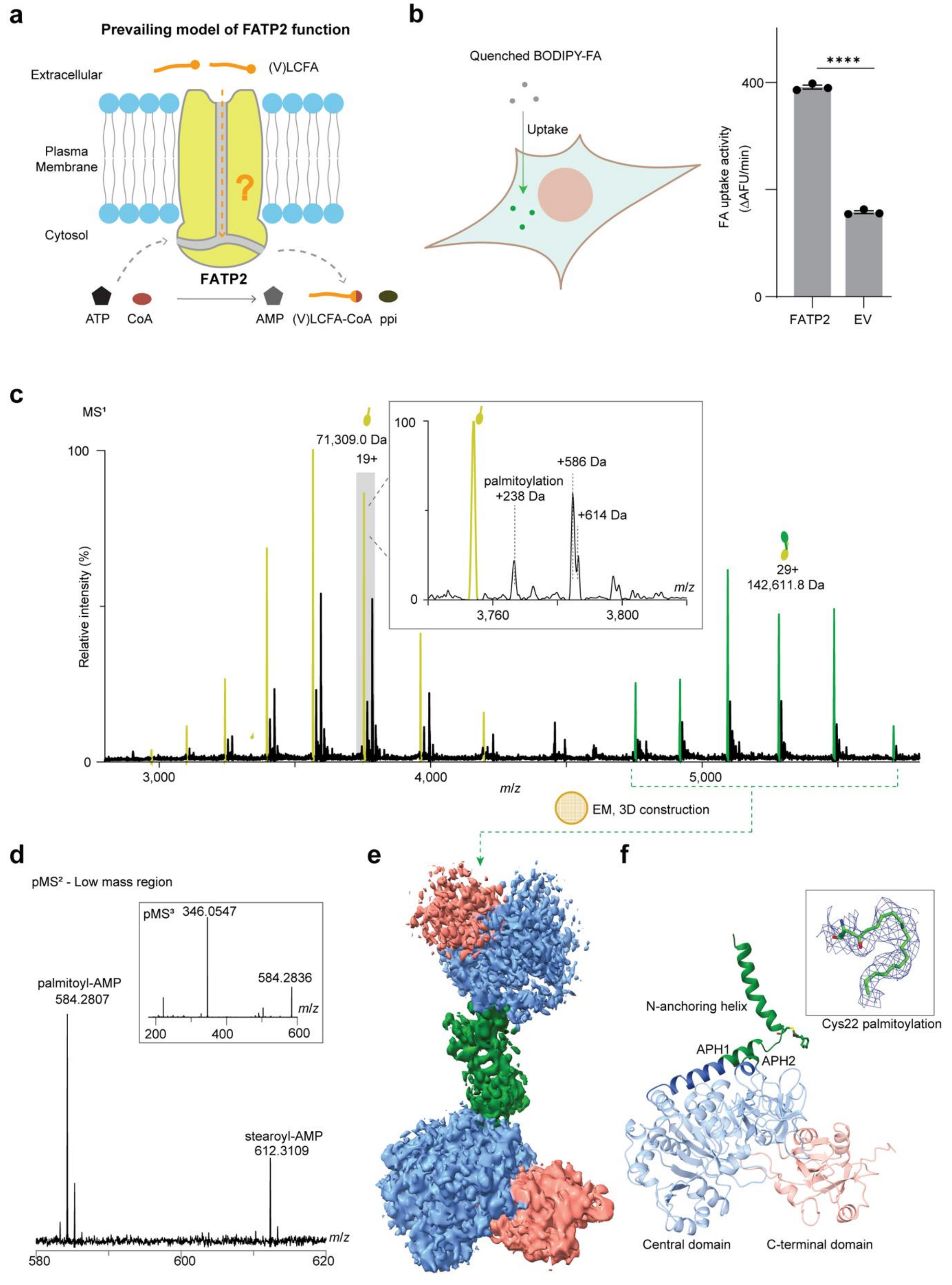

Fig. 1. Functional properties of human FATP2. **a**, Prevailing model of FATP2 function. FATP2 has been proposed to function both as a transporter that directly translocates long- and very-long-chain fatty acids ((V)LCFAs) across the membrane, and as an enzyme that activates (V)LCFA into fatty acyl-CoA. The mechanistic basis of this proposed dual transport-activation function remains unresolved. **b**, Cell-based

fatty acid uptake assay. BODIPY-labelled fatty acids were added extracellularly and remained quenched until internalized by HEK293T cells. Overexpression of FATP2 significantly increases BODIPY-FA uptake relative to empty vector (EV) controls. AFU, arbitrary fluorescence unit. Data are mean ± SEM (n = 3 biological replicates). **** $p \leq 0.0001$, one-way ANOVA with Dunnett's comparisons test (GraphPad Prism 10.5). **c**, Native mass spectrometry (nMS) of purified FATP2. nMS spectrum showing monomeric (yellow) and dimeric (green) charge state distribution. Inset shows an expanded view of the 18+ monomeric charge state, with satellite peaks corresponding to palmitoylation and fatty acyl-adenylate adducts. **d,** Pseudo-MS^2 analysis of FATP2-bound intermediate. Pseudo-MS^2 spectrum following in-source activation and high-energy collision dissociation, yielding fragment ions consistent with adenosine monophosphate (AMP). Inset shows a pseudo-MS^3 spectrum confirming AMP identity. **e**, Cryo-EM map of detergent-solubilized FATP2 showing an antiparallel dimer. **f**, Structural model of FATP2. Cartoon representation showing domain organization, including the N-terminal anchoring helix (green), central domain (sky blue), and C-terminal domain (salmon). Amphipathic helix I (APH1) and amphipathic helix II (APH2) are indicated. Inset shows EM density (contoured at 5σ) corresponding to a covalently attached palmitoyl group at Cys22.

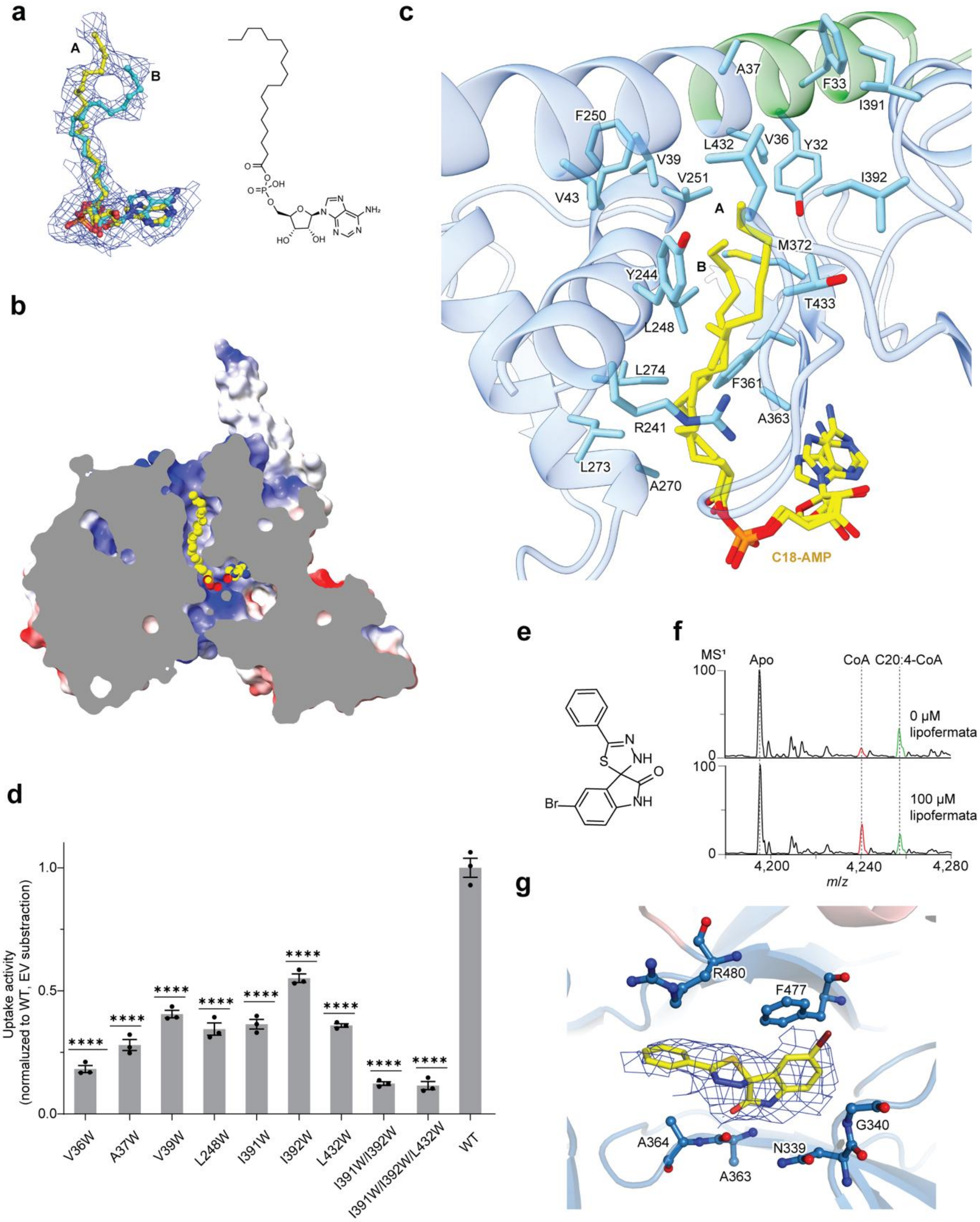
a
A
B
O
P
OH
O
O
N
N
N
N
NH₂
HO
OH
b
c
A37
F33
I391
F250
L432
V36
Y32
V39
V251
I392
V43
A
M372
B
Y244
T433
L248
L274
F361
R241
A363
L273
A270
C18-AMP
d
Uptake activity
(normaluzed to WT, EV substraction)
1.0
0.5
0.0
****
V36W
A37W
V39W
L248W
I391W
I392W
L432W
I391W/I392W
I391W/I392W/L432W
WT
e
N
NH
S
O
NH
Br
f
MS¹
Apo
CoA
C20:4-CoA
100
0
0 μM lipofermata
100 μM lipofermata
4,200
4,240
4,280
m/z
g
R480
F477
G340
A364
N339
A363

Fig. 2. Structural basis of fatty acid entry, activation, and inhibition by FATP2. a, Cryo-EM density (contoured at 3σ) corresponding to stearoyl-adenylate (C18:0-AMP) modelled in two conformations within the substrate-binding tunnel. **b,** Cutaway surface coloured by Coulombic electrostatic potential highlighting the membrane-facing substrate tunnel (red, negative: white, neutral; blue, positive). **c**, Close-up view of the fatty acid binding tunnel showing residues lining the entry and interior. **d,** Fatty acid uptake in HEK293T cells expressing FATP2 tunnel variants. Uptake values are shown after subtraction of empty vector (EV) baseline and normalization to protein expression levels. WT, wild type. Data are mean ± SEM (n = 3 biological replicates). ****p ≤ 0.0001, ordinary one-way ANOVA with Dunnett's multiple comparisons test (Graphpad Prism 10.5). **e**, Chemical structure of FATP2 inhibitor Lipofermata. **f**, nMS analysis of FATP2 incubated with arachidonic acid (C20:4) and CoA in the presence or absence of Lipofermata, showing reduced acyl-CoA production upon inhibitor treatment. Inset shows quantification of C20:4-CoA production, expressed as the intensity of the C20:4–CoA adduct relative to total CoA species. Data are mean ± SEM (n = 3 biological replicates). **g**, Cryo-EM density (contoured at 3σ) and binding mode of Lipofermata within the adenylate binding pocket of FATP2.

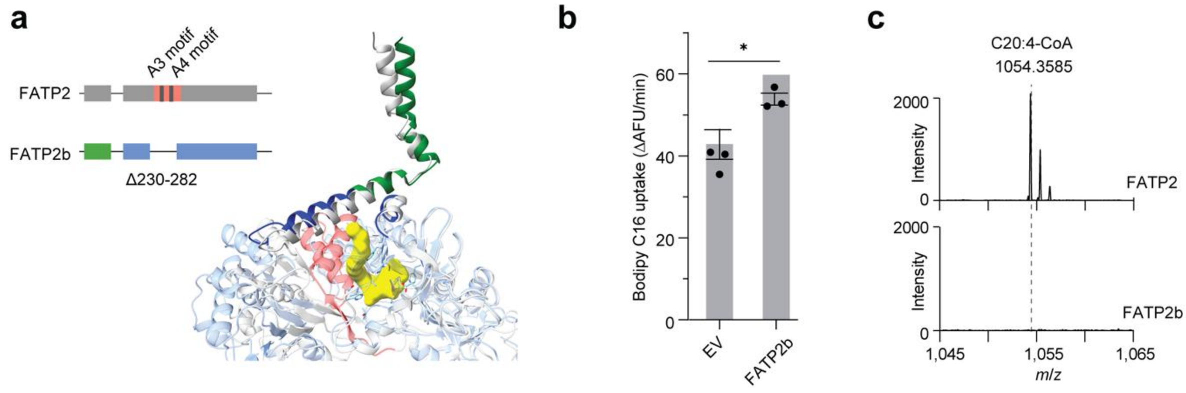

Fig. 3. FATP2b retains uptake activity while being catalytically inactive. a, Superimposition of AlphaFold3-predicted structure[70] of FATP2b (Δ230-282) with the FATP2-C18:0-AMP structure**.** The missing region in FATP2b is shown in pink. Amphipathic helices (APH1 and APH2, blue) and the-terminal anchoring helix (green) remain structurally conserved in the FATP2b model. **b,** Fatty acid uptake in cells expressing WT FATP2 and FATP2b, normalized to WT protein expression levels and shown relative to empty vector (EV). ****p ≤ 0.0001, two-tailed t-test with Welsh's correction. Data are mean SEM (n = 3 biological replicates). **c**, Low mass range region of MS spectrum for quenched reaction mixtures containing FATP2 or FATP2b incubated with C20:4, CoA, $MgCl_2$, and ATP, showing reduced acyl-CoA product formation by FATP2b.

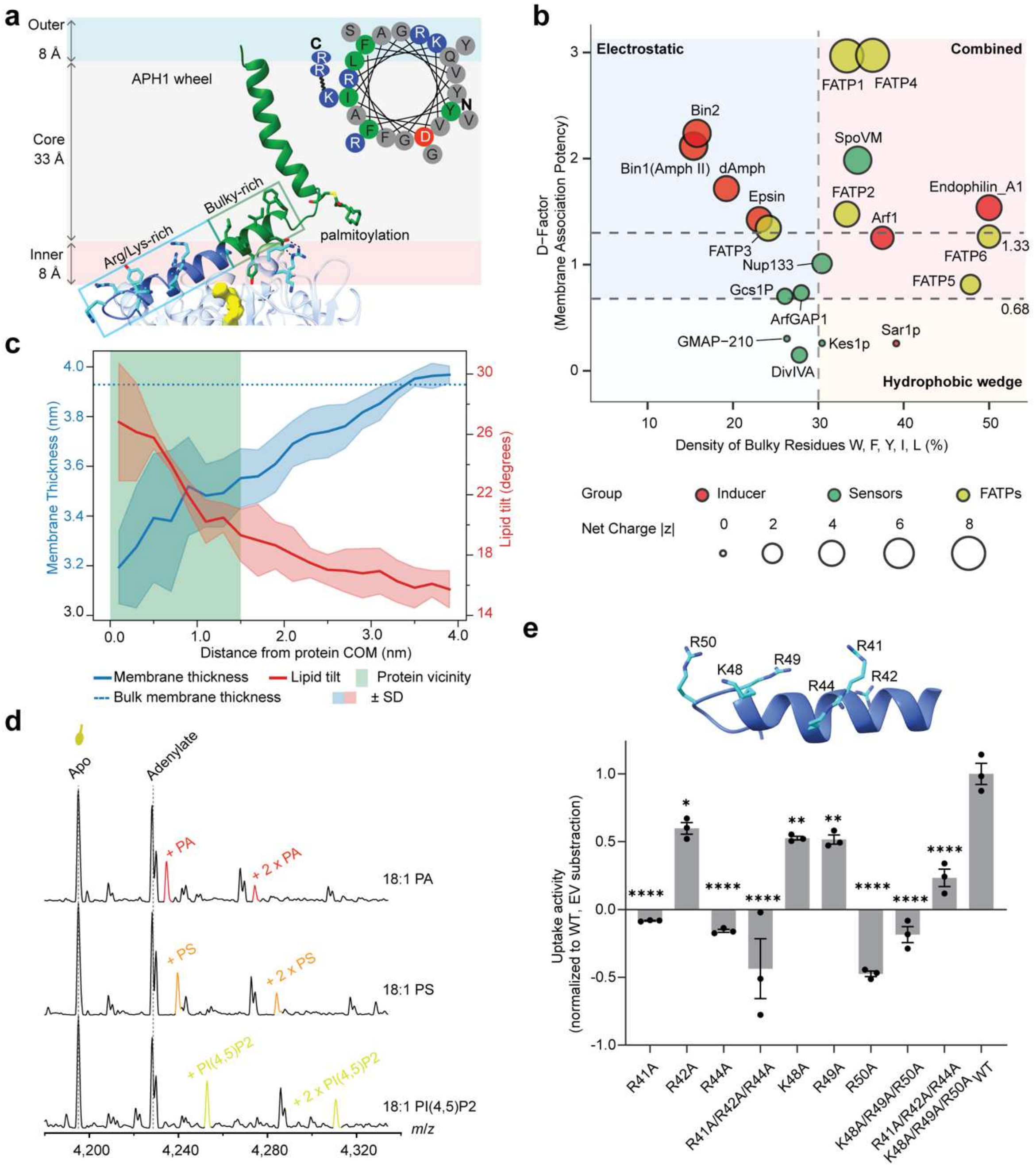

Fig. 4. Amphipathic helices perturb lipid packing defects and regulate fatty acid uptake. **a**, Model of FATP2 positioned at the cytosolic leaflet based on OPM/PPM analysis[36], highlighting APH1 and APH2. Inset, helical wheel projection[71] of APH1 showing segregation of hydrophobic and basic residues. **b**, Scatter plot of discrimination factor (D-factor) versus bulky residue density for APH1s from FATPs (yellow), reference curvature sensors (green), and curvature inducers (red). Dashed lines denotes thresholds for curvature inducer ($D > 1.33$)[71] and hydrophobic wedge effect (>30%)[67]. **c,** Molecular dynamics simulation of FATP2 in ER-mimetic membrane showing local membrane thinning and lipid tilting adjacent to the amphipathic helices. **d,** nMS showing association of FATP2 with anionic phospholipids, including phosphatidic acid (PA), phosphatidylserine (PS), and phosphatidylinositol 4,5-bisphosphate ($\mathrm{PI(4,5)P_2}$). **e,** Fatty acid uptake in cells expressing APH1 variants,

shown after subtraction of empty vector baseline and normalization to protein expression levels. Mutations of basic residues in the C-segment of APH1 reduce uptake. Data are mean SEM (n = 3 biological replicates). Data are mean ± SEM (n = 3 biological replicates). $^{*}P \leq 0.05$; $^{**}P \leq 0.01$, $^{***}P \leq 0.001$; $^{****}P \leq 0.0001$, one-way ANOVA with Dunnett's multiple comparisons test (Graphpad Prism 10.5).

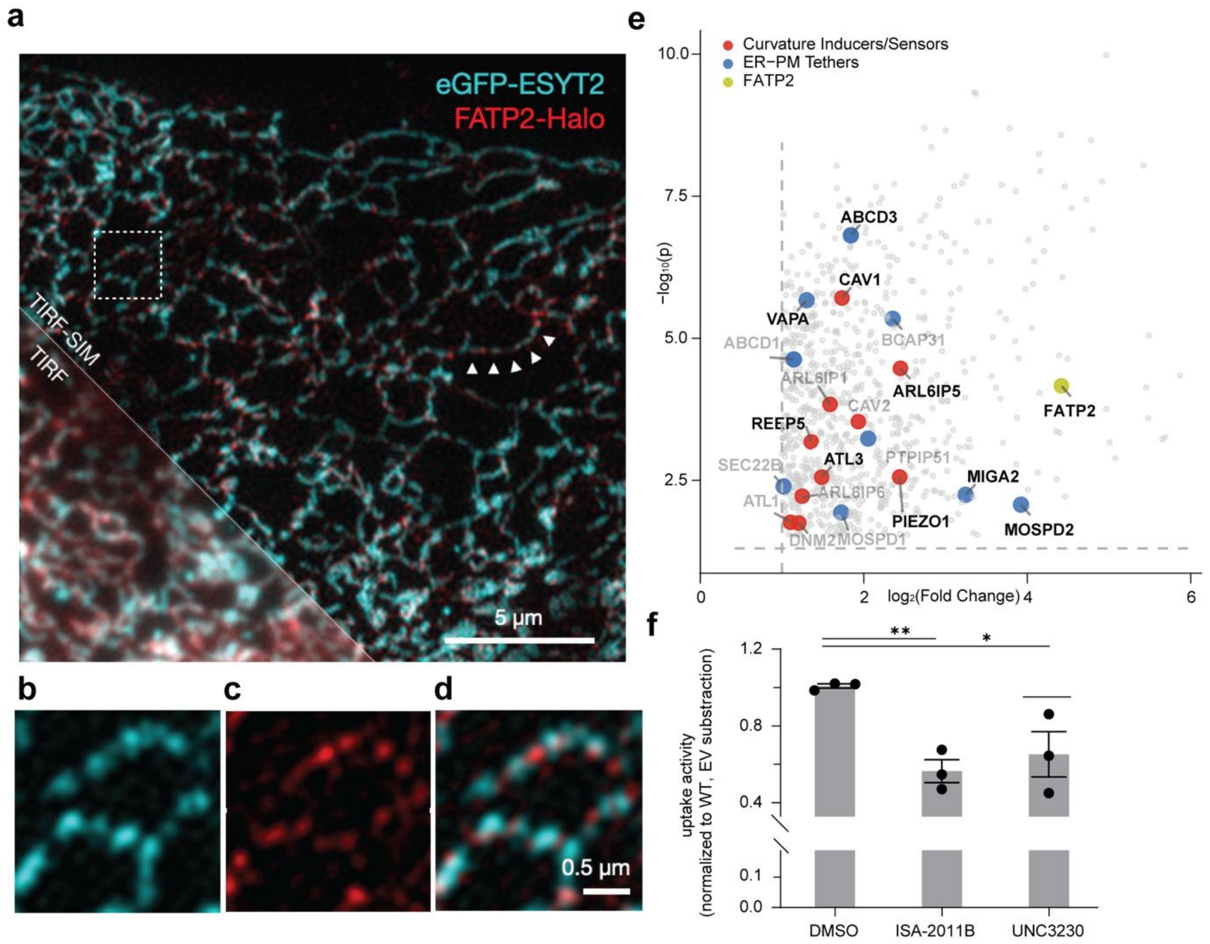

Fig. 5. FATP2 associates with ER–plasma membrane contact site to support fatty acid uptake. **a,** TIRF-SIM imaging of U2OS cells co-expressing FATP2-Halo and eGFP-ESYT2, showing punctate FATP2 assemblies along the cortical ER network. Lower left corner shows conventional TIRF resolution for comparison. **b-d,** Enlarged view of boxed region in (a) showing FATP2-Halo (**b**), EGFP-ESYT2 **(c),** and merged channel **(d). e,** Volcano plot of proteins enriched in anti-FLAG immunoprecipitates from HeLa cells expressing FATP2-FLAG, determined by label-free quantitative proteomics (n = 4 biological replicates; two-tailed t-test). Proteins are color-coded by functional class: curvature-associated proteins (red), ER-organelle tethers (blue), and other-enriched proteins are shown in light grey. **F,** Fatty acid uptake in HEK293T cells expressing FATP2 following pharmacological perturbation of $PI(4,5)P_2$ levels using ISA-2011B or UNC3230, with DMSO as a control. Uptake values are normalized to DMSO-treated cells after subtraction of the empty vector baseline. Data are mean ± SEM (n = 3 biological replicates). $^*P \leq 0.05$; $^{**}P \leq 0.01$; ns, not significant; one-way ANOVA with multiple comparisons relative to DMSO controls.

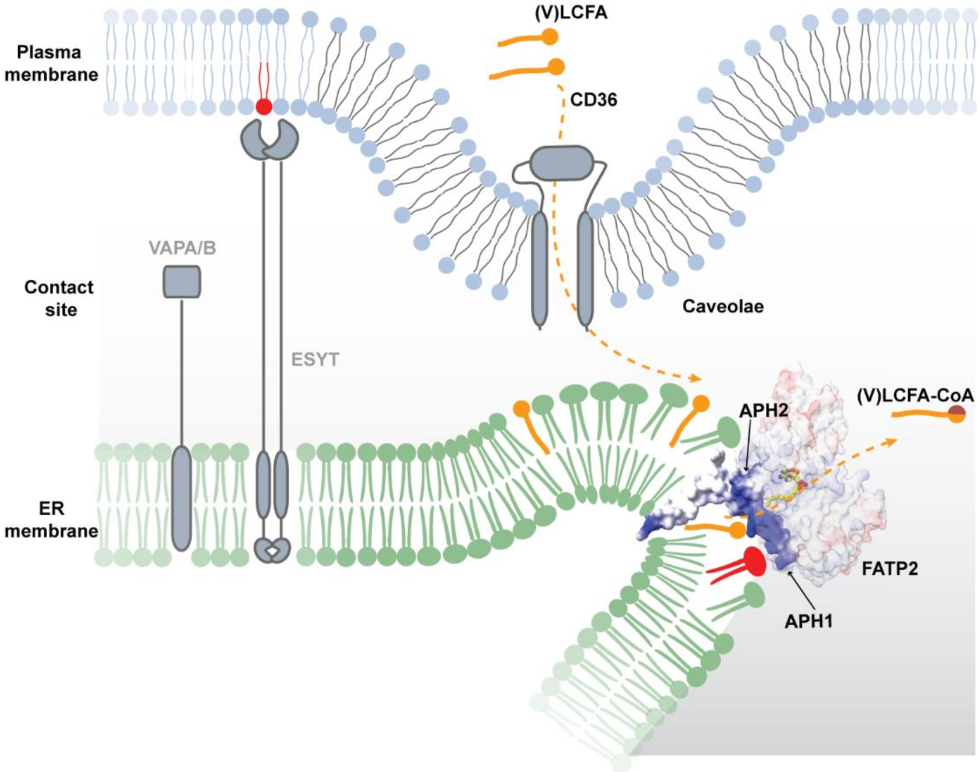

Fig. 6. Model for fatty acid uptake and activation enabled by the amphipathic helices of FATP2 at ER–PM contact site. Schematic model illustrating fatty acid uptake at ER–plasma membrane interfaces. (V)LCFAs inserts into plasma membrane, aided by caveolae and cell surface receptor CD36. At ER–PM interfaces stabilized by tethering proteins (for example, ESYT2 and VAPB), the closely apposed membranes create a shared cytosolic interface. FATP2 engages the cytosolic leaflet of ER membrane via amphipathic helices (APH1 and APH2), forming a membrane-interfacial substrate entry pathway. Molecular simulations indicate that these helices locally perturb lipid packing, which may lower the energetic barrier for both insertion into and extraction at the contact site, thereby facilitating movement of fatty acids into the FATP2 entry tunnel. Extracted substrates are subsequently activated to acyl-CoA within the catalytic pocket. The retention of uptake activity in catalytically inactive FATP2b supports a role for membrane engagement in promoting fatty acid capture independent of immediate adenylation. (V)LCFAs are shown in orange, and negatively charged lipids are shown in red.

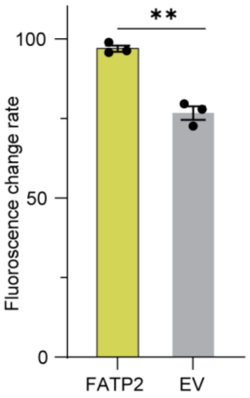

Extended Data Fig. 1. FATP2 overexpression in HeLa cells promotes fatty acid uptake. Uptake velocity is measured by monitoring the fluorescence following incubation with Bodipy FL C16. AFU, arbitrary fluorescence unit; EV, empty vector. Data are mean ± SEM (n = 3 biological replicates). ** p ≤ 0.01, by an unpaired t-test with Welch's correction (Graphpad Prism 10.5).

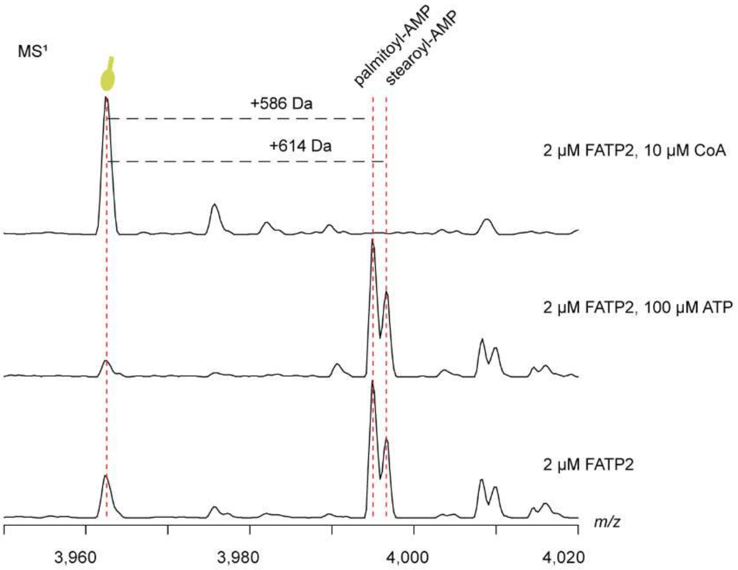

Extended Data Fig. 2. nMS shows depletion of adenylate adducts upon incubation with CoA. Native mass spectra of 18+ charge state of monomeric FATP2 following incubation with ATP or CoA. FATP2 was buffered exchanged into ammonium acetate buffer and incubated with either ATP or CoA for 10 min at room temperature before being analysed for native mass spectrum analysis.

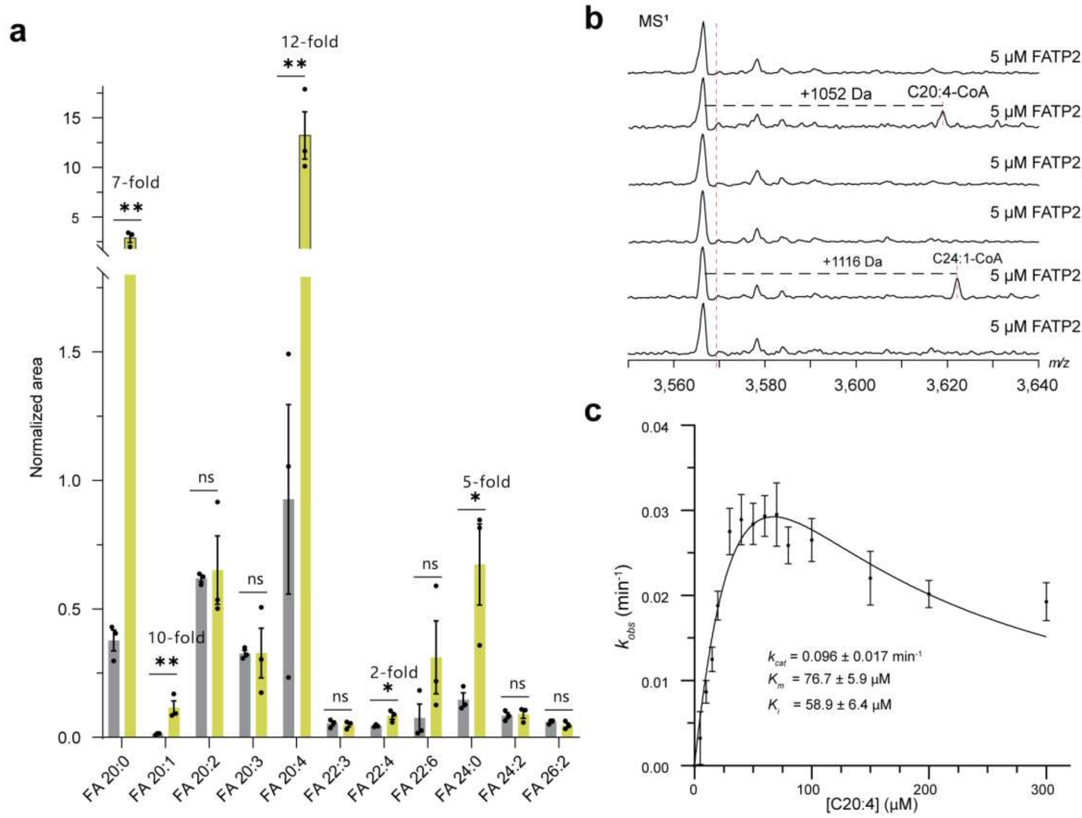

Extended Data Fig 3. FATP2 prefers unsaturated fatty acids. a. Lipidomic analysis on purified FATP2 revealed enrichment of (V)LCFAs compared to crude membrane. Data are mean ± SEM (n = 4 biological replicates). $^*p \leq 0.05$, $^{**}p \leq 0.01$, ns, not significant, by an unpaired t-test with Welch's correction (Graphpad Prism 10.5). **b.** Native mass spectra of 20+ charge state of FATP2 following incubation with a panel of saturated and unsaturated fatty acids. **c.** Steady-state kinetics of FATP2 with arachidonic acid as substrates. Pyrophosphate release from ATP consumption was monitored using EnzChek pyrophosphate assay kit. Data are shown as averaged fits for visualization; kinetic parameters were obtained by separate fits of three independent experiments (biological replicates) using built-in substrate-inhibition equation in Graphpad Prism 10.5. Quantification of pyrophosphate was calibrated against a pyrophosphate standard curve.

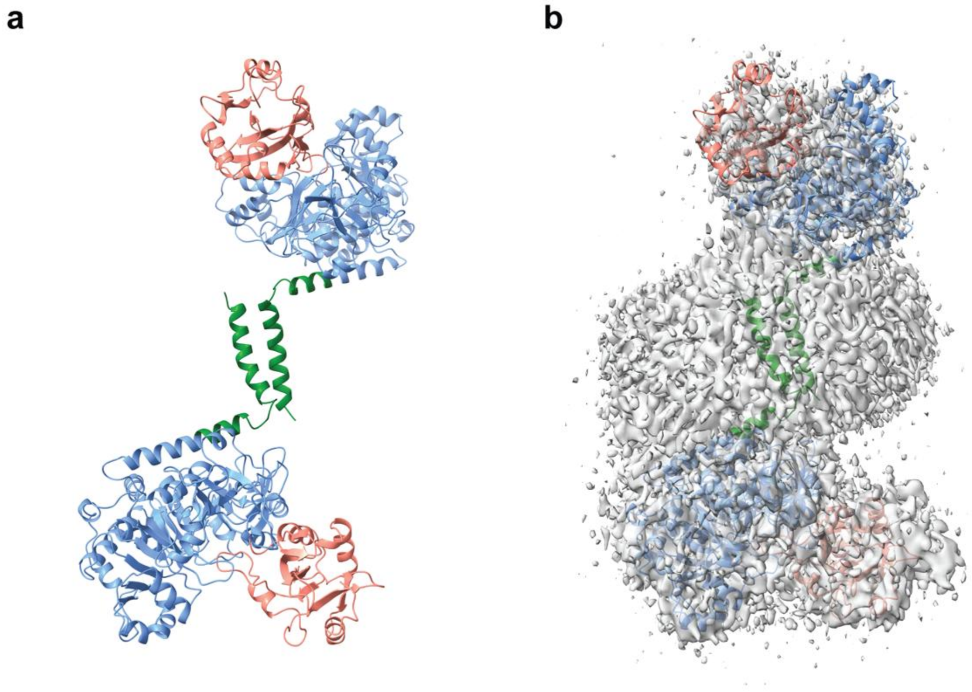

Extended Data Fig. 4. **Cryo-EM structure showing anti-parallel dimer of FATP2.** **a.** Overall cartoon structure of FATP2 dimer showing the catalytic central domain (blue) and C-terminal domain (salmon) from individual protomers. The dimer interface is formed purely by N-terminal anchoring helix (1-22). **b.** Cryo-EM map the FATP2 anti-parallel dimer.

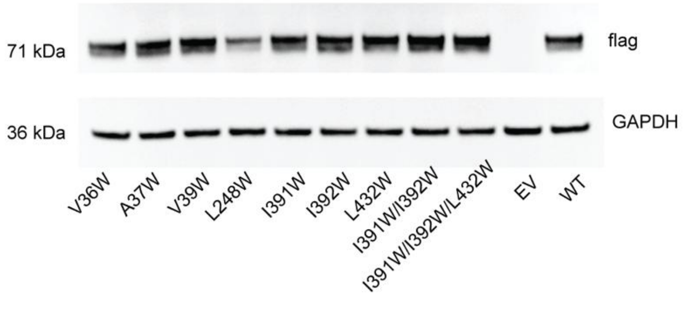

Extended Data Fig. 5 Western-blot analysis FATP2 tunnel variants expressed in HEK293T cells. WT, wild type; EV, empty vector. GAPDH serves as a loading control. Relative band intensities were quantified using ImageJ. Three independent experiments were performed.

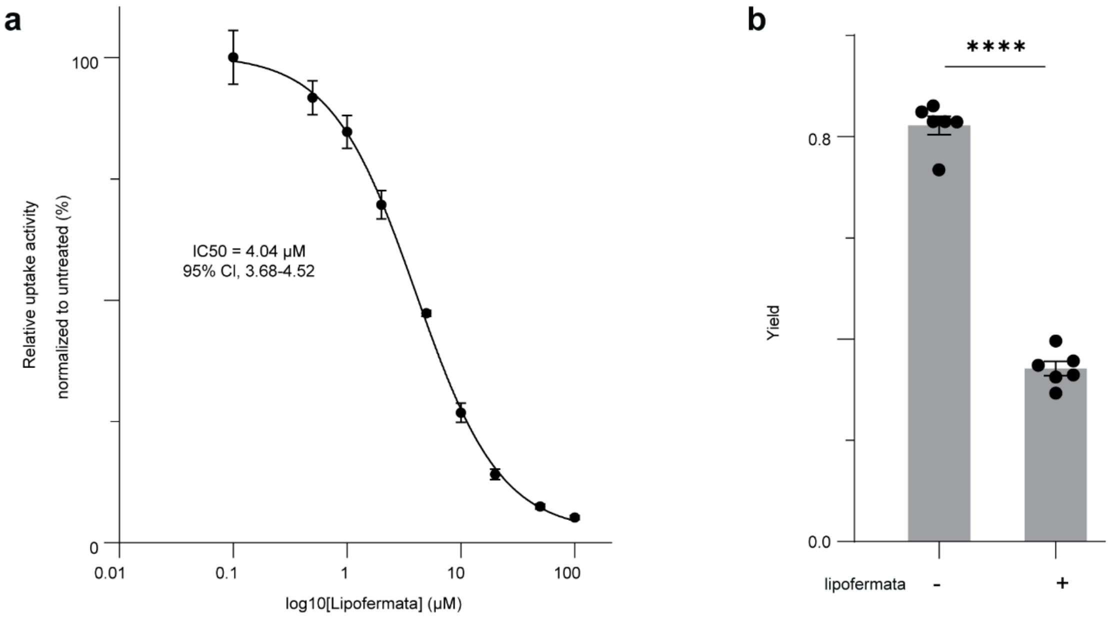

Extended Fig. 6 Lipofermata inhibits FATP2-mediated fatty acid uptake and enzymatic activity. a. Dose-response curve for Lipofermata in HEK293T cells expressing wild type FATP2. Uptake activity (without subtraction of empty vector baseline) was normalized to untreated FATP2-expressing cells. Data are mean ± SEM (n = 3 biological replicates). **b.** Quantification of C20:4-CoA production, expressed as the intensity of the C20:4–CoA adduct relative to total CoA species. Lipofermata decreased product yield by ~2-fold. Data are mean ± SEM. ****$P \leq 0.0001$, two-tailed unpaired t-test with Welch’s correction (GraphPad Prism 10.5).

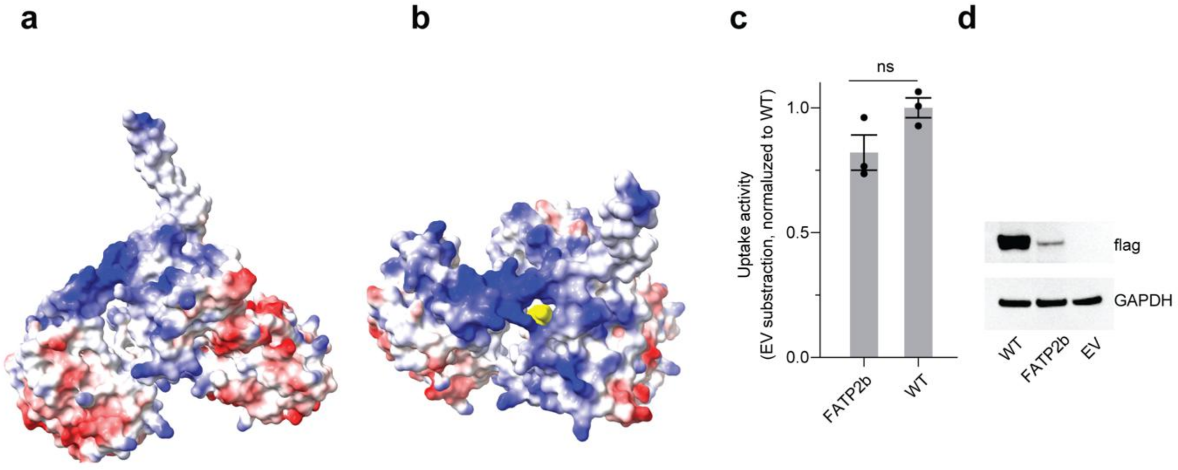

Extended Data Fig 7. FATP2b retains uptake activity comparable to wild type. a-b. Coulombic electrostatic surface representation (side view and top view of substrate entry tunnel) of FATP2b calculated in ChimeraX**.** Positive, neutral and negative electrostatic potentials are shown in blue, white and red, respectively. Adenylate intermediate in yellow is *in silico* modelled in predicted FATP2b structure by superimposition to FATP2 adenylate complex structure. **c.** Raw fatty acid uptake in cells expressing FATP2b and the empty vector. Data are mean SEM (n = 3 biological replicates). *P ≤ 0.05, two-tailed unpaired t-test with Welch's correction (GraphPad Prism 10.5). **d.** Western-blot analysis FATP2b and wild type in HEK293T cells. WT, wild type; EV, empty vector. GAPDH serves as a loading control. Relative band intensities were quantified using ImageJ. Three independent experiments were performed.

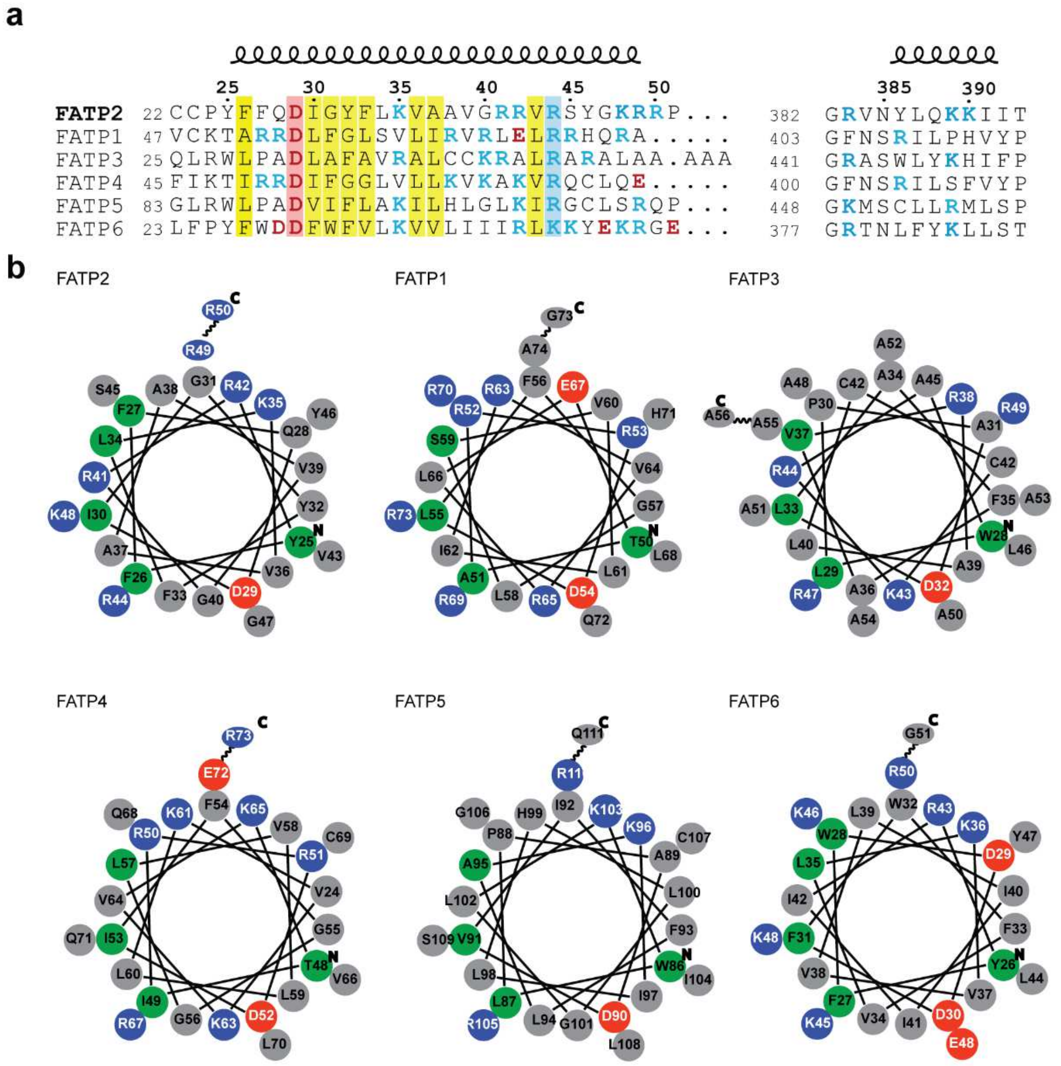

Extended Data Fig 8. Analysis of APH1 and APH2 in FATP family proteins. a. Structural based sequence alignment of AH1 across all six FATPs using AlphaFold models showing dense bulky residues at N-terminal fragment and dense basic residues at the C-terminal fragment. Conserved hydrophobic residues are highlighted in gray; Lys/Arg in blue, Asp/Glu in red. **b**. Helical wheel projection of the APH1 for FATPs, showing clustering of positively charged residues on one face.

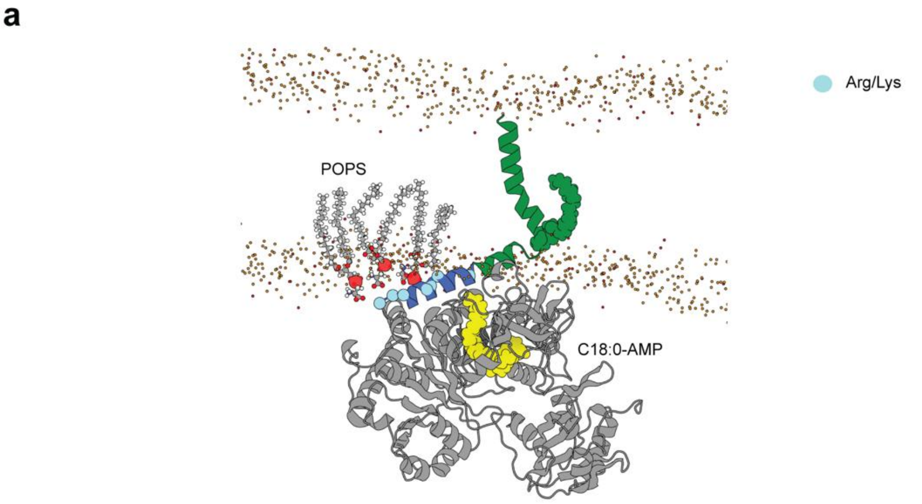

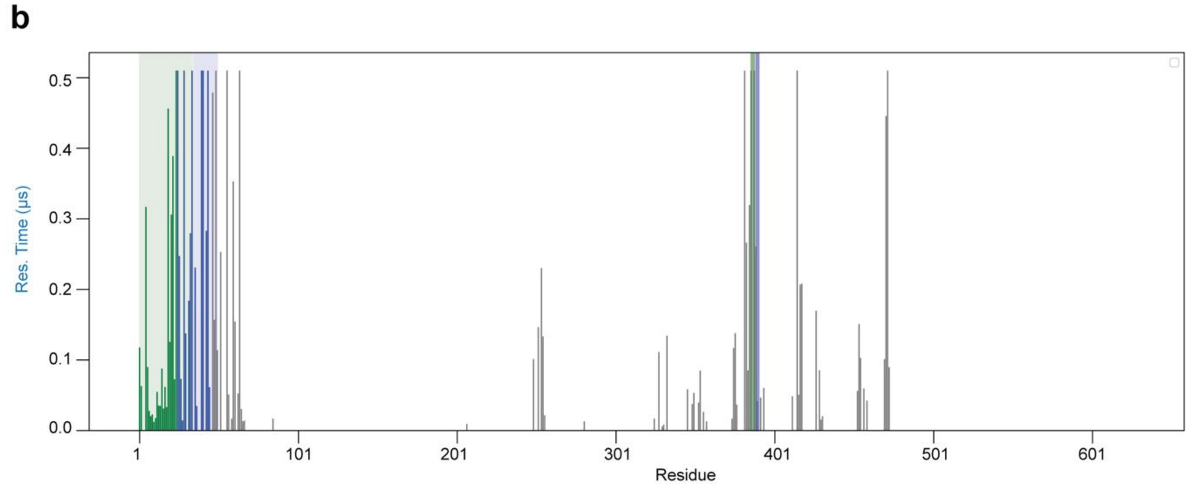

Extended Data Fig 9. MD simulation shows FATP2 interacts with POPS. a. Representative snapshot of FATP2 positioned at the cytosolic leaflet of an ER-like bilayer with N-segments of APH1 and APH2 shallowly penetrating into lipid bilayer while C-segment interacts with POPS. **b.** Residence time of POPS shows preferred interaction with both APHs with FATP2.

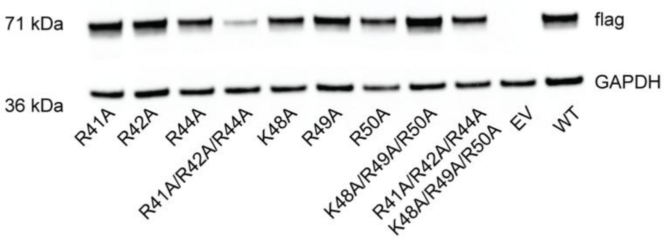

Extended Data Fig 10. Western-blot analysis FATP2 APH variants expressed in HEK293T cells. WT, wild type; EV, empty vector. GAPDH serves as a loading control.

Relative band intensities were quantified using ImageJ. Three independent experiments were performed.

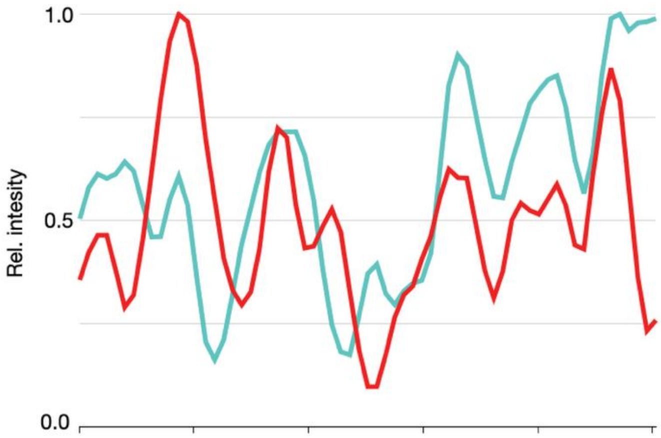

Extended Data Fig. 11. Curvilinear profile plot showing partial overlapping between FATP2 and ESYT2. The plot area is along the ER filament indicated by the arrowheads in **Fig 4a**. Red is FATP2-Hao and cyan is eGFP-ESYT2.

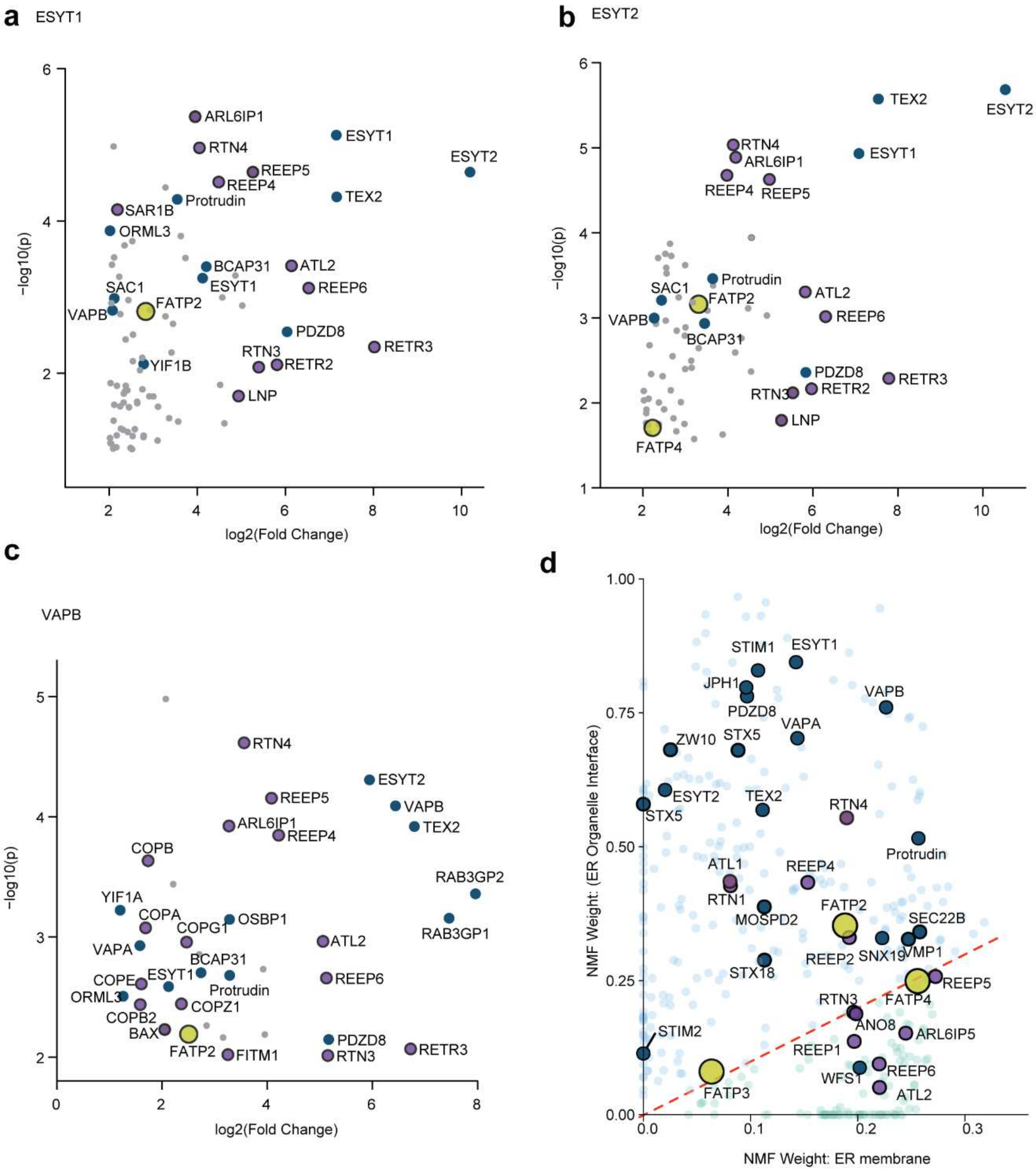

Extended Data Fig 12. (a-c) Volcano plot from published datasets (Bezawork-Geleta et al. Nat. Commun. 2025, 16, 2135)[52] showing proteins including FATP2 that are associated with ER tethers, ESYT1 (**a**), ESYT2 (**b**), and VAPB (**c**). ER shapers, tethers and FATPs are coloured purple, blue and yellow, respectively. **d.** Non-negative matrix factorization (NMF) from published proximity labelling datasets (Go et al. Nature 2021, 595, 120–124) from a BioID map of the HEK293 proteome[53]. Each point represents an ER-localized protein projected according to its relative NMF weights for two spatial clusters: the ER-organelle interface (y-axis) and ER tubular network (x-axis). This plot defines the spatial partitioning of proteins. The red dashed diagonal line denotes the spatial identity boundary, separating proteins preferentially enriched at ER-organelle interfaces (above the line) from those biased toward the tubular ER network (below the line).

Experiments

Cloning and mutagenesis

E. coli Stellar cells (TaKaRa) were used for cloning and amplification of FATP2 and its variants in pCDNA 3.1+. Site-directed mutagenesis of FATP2 was carried out using a reported protocol[72]. *E. coli* stellar cells were cultured in LB medium at 37 °C.

For cloning and amplification of transfer plasmids (pHR-CMV-TetO2_3C-Twin-Strep_IRES-EmGFP, Addgene plasmid #113884), packaging plasmid (psPAX2, Addgene plasmid no. 12260) and second-generation envelope plasmid (pMD2.G, Addgene plasmid no. 12259) were cloned and amplified in NEB stable *E. coli*. NEB stable *E. coli* cells were cultured in LB medium at 30 °C.

Primers were bought from Integrated DNA Technologies (IDT) or Life Technologies Limited. PCR reactions were performed using Phusion high-fidelity PCR master mix (Thermo Scientific) on a MJ Mini PTC-1148 PCR thermal cycler (Bio-Rad).

Cell culture

HeLa (ATCC-CRM-CCL-2), HEK293T (ATCC-CRL-3216), and HEK293S GntI- TetR cells (ATCC-CRL-3022) were used without authentication. HEK293T Lenti-X cells were obtained from Takara.

Cells were cultured in Dulbecco's Modified Eagle Medium/Nutrient Mixture F-12 (DMEM/F-12; Gibco) supplemented with 10% fetal bovine serum (FBS: Gibco) and maintained at 37 °C with 5% CO_2. HEK293F and HEK293S GntI$^-$ TetR used form protein expression were cultured in FreeStyle 293 Expression Medium (Gibco) in an orbital shaker (130 rpm) at 37 °C and with 8% CO_2.

Protein expression and purification

The full-length *SLC27A2* gene encoding human FATP2 (Uniprot ID: O14975) was synthesized (GenScript) and cloned into pCDNA-3.1+ C-DYK vector in frame with C-terminal FLAG tag. A stable HEK 293S GntI$^-$ TetR cell line expressing C-terminal flag-tagged full length FATP2 was generated as previously described[29]. Basically, the gene encoding C-terminal FLAG tagged full length FATP2 was subcloned into transfer plasmid pHR-CMV-TetO2_3C-Twin-Strep_IRES-EmGFP (Addgene plasmid #113884, a gift from J. Elegheert and R. Aricescu). The transfer plasmid, packaging plasmid (psPAX2, Addgene, #12260), and second-generation envelope plasmid (pMD2.G, Addgene, cat. #12259) were co-transfectted into HEK293T Lenti-X cells. Lentiviral particles were collected and used to infect HEK293S GntI- TetR cells. Polyclonal stable cell populations were enriched using fluorescence-activated cell sorting (FACS) and used for later large-scale protein expression in FreeStyle 293 Expression Medium.

For large scale expression, HEK293S GntI$^-$ TetR cells were grown to a density of 1.5-2.0 M cells/mL before induction with 3 μg/mL tetracycline in an orbital shaker (130 rpm) at 37 °C with 8% CO_2. After 16 h, sodium butyrate was added to a final concentration of 5 mM to boost protein expression. Cells were collected 72 h post-induction and stored at -80 °C until use.

Cell pellets were resuspended in lysis buffer (25 mM HEPES pH 7.4, 150mM NaCl) supplemented with cOmplete Protease inhibitor (Roche) and incubated for 30 min before disruption by a single pass through a microfluidizer (M-110P, Microfluidics) at

20,000 psi. The lysate was clarified by centrifugation at 15,000 × g for 20 min to remove unbroken cells, followed by ultracentrifugation at 175,000 × g for 1.5 h to pellet membranes using an Optima L-90K ultracentrifuge with an SW 32-Ti swinging-bucket rotor.

Membrane pellets were homogenized and solubilized for 1.5 h at 4 °C with gentle rotation in solubilization buffer (25 mM HEPES pH 7.4, 150 mM NaCl, 1% (w/v) DDM, 0.1% (w/v) CHS and protease inhibitor). Insolubilized material was removed by centrifugation at 175,000 × g for 30 min, and the supernatant was incubated with pre-equilibrated Pierce anti-FLAG magnetic agarose beads for 1 h at 4 °C. The resin was washed with wash buffer (25 mM HEPES pH 7.4, 150 mM NaCl, 0.03% DDM, and 0.003% CHS), followed by washing with wash buffer supplemented with 5 mM ATP (pH 7.0) and 5 mM $MgCl_2$, and a final wash to remove excess of ATP and $MgCl_2$. Protein was eluted with washing buffer supplemented with 0.2 mg/mL 3×Flag peptide.

Eluted protein was concentrated using concentrator (100 kDa cut-off, Sartorius) and further purified by size exclusion chromatography on a Superdex 200 10/300 GL column (GE Healthcare) equillibrated in buffer containing 25 mM HEPES pH 7.4, 150 mM NaCl, 0.02% DDM and 0.002% CHS. Peak fractions were pooled and concentrated for subsequent experiments. Protein concentrations were determined using NanoDrop One (Thermo Scientific).

Cell-based fatty acid uptake assays.

HEK293T cells were seeded in 12-well plates at a density of 2.5 x 10^5 cells per well in 1000 mL of DMEM/F-12 medium with 10% FBS and incubated overnight in an incubator at 37 °C with 5% CO_2 until reaching 70-80% confluence. Cells were transfected with plasmids encoding full-length wild-type FATP2 or its variants (1 μg per well) using 3 μL FuGENE 6 transfection reagent (Promega) and incubated for 40 hours at 37 °C with 5% CO_2. Cells were subsequently trypsinized, resuspended into DMEM/F-12 medium with 10% FBS, and counted using Countless 3 Automated Cell Counter (Thermo Scientific). Cells were then re-seeded in triplicate at a density of 3.5 x 10^5 cells per well in 96-well plate (back-wall, clear bottom, coated with poly-D-lysine) and incubated overnight at 37 °C with 5% CO_2.

Cells were washed with Hank's Balanced Salt Solution (HBSS) buffer and serum-starved in serum-free DMEM (Gibco) for 2 h. Starved cells were washed with warm HBSS to remove residual serum. Fatty acid uptake was initiated by incubating cells in HBSS buffer containing 2 μM BODIPY FL C16, 0.1% (w/v) fatty acid-free BSA, and 0.05% (w/v) trypan blue. Fatty acid uptake kinetics were monitored by measuring the fluorescence signal (excitation at 485 nm and emission at 520 nm) using ClarioStar plate reader (BMG Labtech) in bottom-read mode. Background fluorescence was subtracted using un-transfected HEK293T cells under identical conditions. Fluorescence intensity was reported as relative fluorescence unit (RFU) and the fatty acid uptake assay was determined by calculating the RFU change rate.

For inhibition assays, HEK293T cells were cultured and transfected with wild-type FATP2 plasmid as described above. 40 h post-transfection, cells were washed with HBSS, serum-starved, and incubated with increasing concentrations of Lipofermata (Cambridge Bioscience) in HBSS for 30 min at 37 °C. Following removal of the supernatant, cells were incubated with fresh HBSS buffer containing 2 μM BODIPY FL

C16, 0.033% (w/v, 5 µM) fatty acid-free BSA, 0.05% trypan blue and the corresponding concentration of Lipofermata. Fatty acid uptake was monitored using the ClarioStar plate reader, and data were analysed using GraphPad Prism 10.5.

For PIP_2 depletion experiments, HEK293T cells overexpressing FATP2 or empty vector were serum-starved and then treated with 50 µM ISA-2011B (Cambridge Bioscience), 50 µM UNC3230 (Cambridge Bioscience) for 2 h, or 5 µM wortmannin (Fisher Scientific) for 30 min at 37 °C. Following inhibitor treatment, cells were washed and fatty acid uptake was initiated by incubation in HBSS containing 2 µM BODIPY FL C16, 0.1% fatty acid–free BSA, 0.05% trypan blue, and the corresponding inhibitor (50 µM ISA-2011B, 50 µM UNC3230, or 0 µM wortmannin). Uptake velocities were quantified using GraphPad Prism 10.5.

In vitro activity assay

Fatty acid activation activity was measured using the EnzChek™ Pyrophosphate Assay Kit (Life Technologies), which detects pyrophosphate released during the reaction. For a typical 50 µL reaction, 0.25 µM FATP2 was incubated in assay buffer (50 mM HEPES, pH 7.4, 150 mM NaCl, 0.03% DDM, 0.003% CHS) containing 0.5 mM ATP, 1 mM $MgCl_2$, 0.5 mM free CoA, 15 mU inorganic pyrophosphatase, 50 mU purine nucleoside phosphorylase (PNP), and 0.2 mM MESG. Reactions were monitored continuously by measuring absorbance at 360 nm in 96-well plates at 25 °C using a FLUOstar plate reader (BMG Labtech). Pyrophosphate concentrations were quantified by comparison with a standard curve.

For *in vitro* inhibition assays, 2 µM FATP2 was incubated with 20 µM arachidonic acid (C20:4), 20 µM ATP, 20 µM CoA, and 1 mM $MgCl_2$ in 0.5 M ammonium acetate buffer containing 0.16% (w/v) DM, in the presence or absence of 100 µM Lipofermata. After 10 min incubation, reaction mixtures were analysed by native mass spectrometry. Reactions were additionally quenched by addition of 5% (v/v) formic acid, and production of C20:4–CoA was quantified by mass spectrometry.

For *in vitro* activity assays of FATP2b, 2 µM FATP2b was incubated with 20 µM arachidonic acid (C20:4), 20 µM ATP, 20 µM CoA, and 1 mM $MgCl_2$ in 0.5 M ammonium acetate buffer containing 0.16% DM. After 1 h incubation, reactions were quenched by addition of 5% formic acid, and production of C20:4–CoA was quantified by mass spectrometry.

Immunoblotting

HEK293T cells were transfected with plasmids encoding wild-type FATP2 and its variants using FuGENE 6 transfection reagent in 96 well plates (black wall, clear bottom). Forty hours post-transfection, cells were washed with phosphate-buffered saline (PBS) and lysed in 50 µL RIPA buffer (Life Technologies) supplemented with cOmplete protease inhibitor cocktail (Roche). Lysates were incubated on ice for 30 min with gentle shaking (400 rpm) and sonicated in a cold-water bath for 5 min.

Protein samples were resolved by SDS–PAGE using 4–12% Bis-Tris NuPAGE gels (Invitrogen) and transferred to PVDF membranes using a Trans-Blot Turbo system (Bio-Rad). Membranes were blocked for 1 h at room temperature in Tris-buffered saline with Tween 20 (TBST; 20 mM Tris-HCl, pH 8.0, 150 mM NaCl, 0.1% Tween 20) supplemented with 5% (w/v) non-fat milk (Millipore). Membranes were incubated with primary antibodies diluted in TBST according to the manufacturers' recommendations for 2 h at room temperature, followed by three washes with TBST (5 min each). Membranes were then incubated with horseradish peroxidase (HRP)-conjugated secondary antibodies (Cell Signaling Technology) diluted in TBST for 1 h at room temperature. After three additional washes with TBST, immunoblots were developed using Pierce™ ECL Western Blotting Substrate (Thermo Fisher Scientific). Images were acquired using an iBright CL1500 Imaging System (Thermo Fisher Scientific) and analysed with iBright Analysis Software. Primary antibodies used were: GAPDH (D4C6R) mouse monoclonal antibody (Cell Signaling Technology, cat. #97166); DYKDDDDK tag (D6W5B) rabbit monoclonal antibody (Cell Signaling Technology, cat. #14793); and FATP2/SLC27A2 (E8F8O) rabbit monoclonal antibody (Cell Signaling Technology, cat. #78771). Secondary antibodies used were HRP-linked anti-mouse IgG (Cell Signaling Technology, cat. #7076) and HRP-linked anti-rabbit IgG (Cell Signaling Technology, cat. #7074)

Live cell imaging

U2OS cells (human osteosarcoma cell line; ATCC HTB-96) were cultured in DMEM/F-12 medium supplemented with 10% fetal bovine serum (FBS). For imaging experiments, approximately 2.5 × 10^5 cells were plated in 3 cm^2 glass-bottom dishes (Thermo Fisher Scientific, cat. #150682) and cultured overnight at 37 °C with 5% CO_2. Cells were transfected the following day with 100 ng of FATP2–Halo and EGFP–ESYT2 (Addgene plasmid #66831) using FuGENE HD (Promega) according to the manufacturer's instructions. Prior to imaging, the culture medium was replaced with FluoroBrite DMEM (Life Technologies) supplemented with 20 mM HEPES (pH 7.4). Live-cell imaging was performed using a DeltaVision OMX SR microscopy system (GE Healthcare) equipped with four laser lines (405, 488, 593, and 633 nm), pco.edge 4.2 sCMOS cameras (PCO), and a 60× oil-immersion objective (Olympus UPLAPO, NA 1.5). Cells were maintained at 37 °C with 5% CO_2 in a humidified environmental chamber during image acquisition. Images were reconstructed using DeltaVision softWoRx software, aligned using Chromagnon[73], and further processed using Fiji (version 2.16).

Native mass spectrometry analysis

Purified FATP2 was buffer-exchanged into 500 mM ammonium acetate buffer (pH 7.5) containing 0.16% (w/v) DM using Zeba Spin 40K MWCO desalting column (Thermo Scientific). Protein concentration was determined using NanoDrop and adjusted into desired concentration for native mass spectrometry analysis. Typically, 3 μL of desalted protein was loaded into a gold-coated borosilicate capillary prepared in-house and electrosprayed into a Q Exactive UHMR hybrid quadrupole-Orbitrap mass spectrometer (Thermo Fisher Scientific) with the following settings: capillary voltage of 1.0 kV, UHV pressure of 7.5×10^{-10} mbar, capillary temperature of 200 °C, and resolution of 17,500. Unless otherwise stated, all the experiments were performed in the positive mode. Raw MS data were processed with Xcalibur 4.1.50 (Thermo Scientific). Unidec software v6.0.1[74] was used for spectral deconvolution.

Cryo-EM sample preparation and data acquisition and processing

Purified FATP2 samples at a concentration of 1.6 mg mL^{-1} were applied to freshly glow-discharged Quantifoil R1.2/1.3 300-mesh gold grids and blotted for 3.0 or 3.5 s at 100% humidity, followed by plunge-freezing in liquid ethane using a Vitrobot Mark IV (Thermo Fisher Scientific). For preparation of the Lipofermata-bound complex, FATP2 (1.6 mg/mL) was incubated with 0.5 mM Lipofermata on ice for 1 h prior to plunge-freezing.

Cryo-EM data were collected on a Titan Krios G3 transmission electron microscope (Thermo Fisher Scientific) operated at 300 kV and equipped with a Gatan GIF energy filter and a K3 BioQuantum direct electron detector operating in counting super-resolution mode with 2× binning. Movie stacks were recorded at a nominal magnification of 105,000×, corresponding to a calibrated pixel size of 0.836 Å. Data were collected with a defocus range of −0.8 to −2.0 μm. A summary of cryo-EM data acquisition parameters is provided in Supplementary Table 2.

The datasets were processed using *CryoSPARC*[75]. Dose-fractionated movie frames were aligned using patch motion correction, and contrast transfer function (CTF) parameters were estimated using patch CTF estimation. Particles were automatically picked using template-based picking and initially extracted with 6× binning using cryoSPARC Live. Several rounds of two-dimensional (2D) classification were performed to remove poorly aligned or heterogeneous particles. Selected particles were subsequently re-extracted with 1.5× binning, corresponding to a final pixel size of 1.0 Å per pixel.

A total of 376,327 particles for the C18:0–AMP-bound dataset and 183,980 particles for the Lipofermata-bound dataset were subjected to heterogeneous refinement. Following classification, 211,297 and 135,106 particles were selected for further refinement of the C18:0–AMP and Lipofermata datasets, respectively. Multiple rounds of local refinement were performed, and a local mask encompassing a single protomer was applied during the final refinement. The final reconstructions reached overall resolutions of 3.68 Å for the C18:0–AMP-bound structure and 3.80 Å for the Lipofermata-bound structure, as determined by the gold-standard Fourier shell correlation (FSC) criterion at 0.143. Local resolution estimates were calculated in cryoSPARC.

Model building and refinement

An initial model of FATP2 was obtained from AlphaFold Protein Structure Database. The model was rigid-body fitted into the EM density maps using UCSF ChimeraX-V1.9. The generated model was refined against the corresponding maps in phenix.real_space_refine. Molprobity[76] were used to guide iterative rounds of model adjustment in Coot v.0.9.8[77] and refinement in Phenix v.1.21.2[78]. Restraint file for Lipofermata was generated using eLBOW in Phenix. All figures were prepared in PyMoL v.3.1.6 (Schrödinger, LLC) or ChimeraX-1.9[79].

Calculation of biophysical properties of amphipathic helices.

Sequences from amphipathic helices for ALPS motif-containing proteins (Gcs1p, DivIVA, GMAP-210, ArfGAP1, Kes1p, Nup133, SpovM) and selected curvature-inducing proteins (Bin2, Bin1, dAmph, Epsin, Arf1, Sar1p, Endophilin A1) were obtained from a previous report[41]. Amphipathic helices from FATP family members were identified by structure-based sequence alignment using MUSTANG[80] and AlphaFold predicted structures[81,82]. Amphipathic sequences for ER shaping proteins (RTNs and REEPs) are determined as reported[48]. Biophysical properties of these amphipathic helices were calculated using the Peptides R package[83]. Mean hydrophobicity (H) and mean hydrophobic moment (μH) were calculated using the standardized Eisenberg consensus scale[84], assuming an ideal α-helical periodicity of 100° per residue. Net charge (z) was calculated as the sum of basic residues (Lys, Arg; +1) and acidic residues (Asp, Glu; -1), assuming a physiological pH of 7.4. Membrane binding and curvature-inducing potential were estimated using the discrimination factor (D) defined by the HeliQuest algorithm[71]:

$D = 0.944 \times \mu H + 0.33 \times z$.

The density of bulky residues was calculated as the percentage of bulky residues (W, Y, F, I, L) within each amphipathic helix sequence.

Molecular dynamic simulations

The system was run simulated in triplicate, and all of replicas—including ligand parameterisation—were prepared using CHARMM-GUI[85,86] with the CHARMM36(m) force field[87] and the TIP3P water model[88,89]. Each replica was simulated for 0.5 μs each, yielding a total aggregated simulation time of 1.5 μs. The membrane consisted of a 200 Å bilayer with asymmetric leaflet compositions. The cytosolic facing leaflet comprised DPPC 50%, POPE 20%, POPS 20%, cholesterol 5%, POPI 5%, whereas the other leaflet comprised DPPC 60%, POPE 25%, POPS 5%, cholesterol 5%, POPI 5%. Sodium chloride was added to neutralise the system and to achieve a bulk salt concentration of 150 mM.

Molecular dynamics simulations were performed with GROMACS v2021.4 simulation suite or later[90-92] under periodic boundary conditions using the Verlet cut-off scheme. Short-range van der Waals interactions employed a force-switch between 1.0 and 1.2 nm, and electrostatics were treated with particle-mesh Ewald[93] with a 1.2 nm real-space cut-off. All bonds involving hydrogen were constrained with LINCS[94,95] , enabling integration time-steps as specified below.

Systems were energy-minimised with the steepest-descent algorithm (5,000 steps; convergence criterion 1,000 kJ mol^{-1} nm^{-1}), followed by restrained equilibration. Two NVT stages (125 ps each, 1 fs time-step) preceded semi-isotropic NPT equilibration (one 125 ps stage at 1 fs, then three 500 ps stages at 2 fs). Positional and dihedral restraints defined by the CHARMM-GUI protocol were gradually relaxed across these steps (backbone/side-chain/lipid force constants decreased across the sequence). Temperature was maintained at 310 K with a velocity-rescale thermostat[96] (τ_t = 1 ps). Pressure was controlled at 1 bar using the C-rescale barostat[97] in a semi-isotropic scheme (τ_p = 5 ps). Production trajectories were run in the NPT ensemble with a 2 fs integration time-step at 310 K and 1 bar, retaining the thermostat and barostat settings above.

Visualisation and image creation were performed with VMD 1.9.3[98] and Protein Imager[99]. Trajectory analyses were carried out using locally developed Python scripts based on the MDAnalysis package[100,101], as well as standard analysis tools implemented in GROMACS.

Membrane thickness was calculated as the distance along the membrane normal between the average z-positions of lipid headgroups belonging to the upper and inner membrane leaflets. Local and radial thickness profiles were obtained by restricting the analysis to lipid headgroups within defined lateral distances from the centre of mass of the transmembrane helix (residues Tyr25–Arg50) and averaging the inter-leaflet distance over concentric annuli in the membrane plane. All thickness measurements were averaged over time and across independent simulation replicas.

Lipid tilt was quantified as the angle between the membrane normal and a vector connecting the phosphate group to the centre of mass of the lipid acyl chains; cholesterol molecules were excluded from this analysis. Radial tilt profiles were computed as a function of the in-plane distance from the centre of mass of the transmembrane helix by averaging lipid tilt angles within concentric annuli in the membrane plane. Absolute values of the cosine of the tilt angle were used to treat both membrane leaflets equivalently.

All spatial distances were computed laterally with respect to the transmembrane helix. The protein vicinity was defined as the region within 1.5 nm from the helix axis, corresponding to the first lipid shell directly interacting with the helix.

Lipidomics

Lipids and fatty acids were extracted from purified protein samples or cell lysate using a previously described methyl-tert-butyl ether (MTBE)/methanol extraction method[33]. Extracted lipids were dried in a fume hood under a nitrogen flow. The dried lipids were resuspended in buffer (80% lipidomics buffer A/20% lipidomics buffer B). For LC–MS/MS analysis, lipids were separated on a C18 column (Acclaim PepMap 100; 75 µm × 150 mm, 3 µm particle size; Thermo Fisher Scientific) using a Dionex Ultimate 3000 UHPLC system. A binary solvent system was used, consisting of buffer A (60% acetonitrile, 40% water, 10 mM ammonium formate, and 0.1% formic acid) and buffer B (90% isopropanol, 10% acetonitrile, 10 mM ammonium formate, and 0.1% formic acid). Eluted lipids were analysed on an Orbitrap Eclipse Tribrid mass spectrometer (Thermo Fisher Scientific) operated in negative mode using data-dependent acquisition. Lipidomics data were processed and analysed in MS-DIAL-5.4[102].

Isolation of FATP2 immunoprecipitates

HeLa cells were seeded in biological replicates (n = 4) in 100-mm culture dishes (Greiner CellStar) at a density of 2.0×10^6 cells per dish in 12 mL of DMEM/F-12 medium supplemented with 10% fetal bovine serum (FBS) and incubated overnight at 37 °C with 5% CO_2. Cells were transfected the following day with plasmids encoding FATP2-FLAG or empty vector (pcDNA3.1+) (10 µg DNA per dish) using 30 µL FuGENE 6 transfection reagent (Promega) and incubated for 48 h at 37 °C with 5% CO_2. Cells were washed twice with ice-cold phosphate-buffered saline (PBS), resuspended in 2 mL ice-cold PBS, pelleted by centrifugation at 500 × g for 10 min, and snap-frozen in liquid nitrogen. Cell pellets were lysed in 1 mL lysis buffer (25 mM HEPES, pH 7.4, 150 mM NaCl, 10% glycerol, 1 mM EDTA, 1% DDM, and 0.1% CHS) supplemented with protease inhibitor cocktail (cOmplete, Roche) and phosphatase inhibitor cocktail (PhosSTOP, Roche). Lysates were gently mixed on a rotating wheel at 4 °C for 1 h and clarified by centrifugation at 18,000 × g for 15 min.

Protein concentrations were determined using a BCA Protein Assay Kit (Pierce, Thermo Fisher Scientific). Equal amounts of protein (~2 mg) were incubated with 25 µL anti-DYKDDDDK magnetic agarose beads (Pierce; A36797) and rotated overnight at 4 °C. Beads were washed three times with ice-cold PBS using a DynaMag-2 magnetic rack (Thermo Fisher Scientific).

Immunoprecipitated proteins were reduced with 5 mM tris(2-carboxyethyl)phosphine (TCEP) for 30 min at 37 °C, followed by alkylation with 10 mM iodoacetamide for 30 min at room temperature in the dark in 50 mM ammonium bicarbonate buffer. Excess iodoacetamide was quenched by incubation with 20 mM dithiothreitol (DTT) for 10 min at room temperature. Beads were washed twice with 50 mM ammonium bicarbonate buffer and resuspended in digestion buffer containing sequencing-grade modified trypsin (Promega). Proteolytic digestion was carried out overnight at 37 °C and quenched by addition of 1% (v/v) formic acid. Peptides were extracted once with 50 µL extraction solution (50% water, 50% acetonitrile, 1% formic acid). Combined extracts were dried using a SpeedVac vacuum concentrator (Thermo Fisher Scientific) and resuspended in 20 µL of solvent containing 95% water, 5% acetonitrile, and 0.1% formic acid. Of this, 10 µL was desalted using C18 ZipTip pipette tips (ZTC18M096; Merck). Eluted peptides were dried and resuspended in a final volume of 20 µL aqueous solution containing 0.1% formic acid for subsequent mass spectrometry analysis.

LC-MS based Proteomics analysis of FATP2 immunoprecipitates

Resuspended peptides were separated via nanoflow reversed-phase liquid chromatography (nanoElute 2, Bruker Daltonics) with a 30 min gradient. 0.5 µL of resuspended peptides were loaded directly onto a 25 cm × 75 µm column packed with 1.7 µm C18 beads (pore size 120 Å; Aurora Ultimate CSI, IonOpticks) and separated at a flow rate of 250 nL/min and a column temperature of 50°C. Buffer A is water with 0.1% formic acid and buffer B consisted of 0.1% formic acid in acetonitrile (v/v; Fisher Scientific, LC-MS grade). The following gradient was used: 2–23% buffer B over 18 min, 23–35% buffer B over 4 min, and buffer 35–90% B over 4 min, followed by a 4-min wash at 90% buffer B. Eluting peptides were infused into a TIMS quadrupole time-of-flight mass spectrometer (timsTOF Ultra, Bruker Daltonics) equipped with an electrospray ion source (CaptiveSpray, Bruker Daltonics). Source parameters were set to a capillary voltage of 1,600 V, a dry gas flow of 3.0 L/min, and a dry gas temperature of 200 °C. Data was acquired in dia-PASEF mode over an m/z range of 400–1,000 and an ion mobility range of $1/K_0$ = 0.64–1.45 Vs/cm^2. The TIMS analyzer was operated at a 100% duty cycle with 100 ms accumulation and 100 ms ramp times (acquisition cycle time = 0.96 s). Collision energies were linearly stepped from 20 to 59 eV as a function of increasing ion mobility.

dia-PASEF raw files were processed using the “DIA_SpecLib_Quant_diaPASEF” workflow in FragPipe[103] v.23.1.52,53 Pseudo-MS/MS spectra were generated using diaTRACER v.1.3.3 and searched using MSFragger v.4.3. Searches were performed against the Homo sapiens UniProt reference proteome (UP000005640; reviewed entries only) supplemented with common contaminants and decoys (downloaded December 2025). Precursor and fragment mass tolerances were set to 20 ppm, and the isotope error window was set to 0/1/2. Mass calibration and parameter optimization were enabled. Enzymatic specificity was set to “stricttrypsin”, allowing up to two missed cleavages. Carbamidomethylation of cysteine was specified as a fixed modification, while methionine oxidation, protein N-terminal acetylation, and pyro-Glu/Gln formation at peptide N-termini were included as variable modifications (maximum of three variable modifications per peptide). MSBooster and Percolator were used to predict retention time and MS/MS spectra, and to rescore peptide–spectrum matches (PSMs). PSMs were filtered to a 1% false-discovery rate (FDR) and combined with the pseudo-MS/MS spectra using EasyPQP v.0.1.52 to generate a spectral library for DIA quantification (139,376 precursors mapping to 8,002 protein groups).

dia-PASEF runs were quantified using DIA-NN v.1.8.2 beta 8[104] with the spectral library generated in FragPipe. Mass accuracy settings for MS^1 and MS^2, as well as the scan window, were determined automatically by DIA-NN based on the first run in the experiment. Precursor and protein group identifications were filtered at 1% FDR. Protein inference was disabled, retaining protein group assignments from the input spectral library. Quantification was performed using fixed-width peak-centre integration. Cross-run normalisation was performed using DIA-NN's default RT-dependent method, and protein group quantities were calculated using the MaxLFQ algorithm. Quantification matrices for precursors, protein groups, and gene groups were exported with 1% FDR filtering. p-values were determined by pairwise Welch's t-test between the control sample and each knockdown condition, using Bonferroni correction to correct for multiple testing.

Re-analysis of published ESYT1, ESYT2 and VAPB immunoprecipitates

Bezawork-Geleta *et al.* previously identified potential interacting proteins for ESYT1, ESYT2, and VAPB using HA-based immunoprecipitation followed by label-free mass-spectrometry[52]. We re-analysed these datasets and replotted volcano plots to highlight proteins of interest, including FATP2 and FATP4, which were enriched in ESYT1, ESYT2, and VAPB immunoprecipitates. Data visualization and statistical analysis were performed using GraphPad Prism version 10.5.

Re-analysis of published proximity labelling shows FATP2 bias toward the ER membrane interface

Go *et al.* generated a human cell map using proximity labelling experiments[53]. Using the non-negative matrix factorization (NMF) profiles provided in Supplementary Table 8A of the original study, we extracted compartment profiles corresponding to rank 15 (nuclear outer membrane–ER membrane network) and rank 3 (ER membrane), which showed the highest enrichment of FATP2. These analyses indicate a preferential association of FATP2 with ER membrane–associated compartments.

1 Shetty, S. S. & Kumari, S. Fatty acids and their role in type-2 diabetes (Review). *Exp Ther Med* **22**, 706 (2021). https://doi.org:10.3892/etm.2021.10138

2 Boden, G. Obesity and free fatty acids. *Endocrinol Metab Clin North Am* **37**, 635-646, viii-ix (2008). https://doi.org:10.1016/j.ecl.2008.06.007

3 Neuschwander-Tetri, B. A. Non-alcoholic fatty liver disease. *BMC Med* **15**, 45 (2017). https://doi.org:10.1186/s12916-017-0806-8

4 Gyamfi, J., Kim, J. & Choi, J. Cancer as a Metabolic Disorder. *Int J Mol Sci* **23** (2022). https://doi.org:10.3390/ijms23031155

5 Jump, D. B. Mammalian fatty acid elongases. *Methods Mol Biol* **579**, 375-389 (2009). https://doi.org:10.1007/978-1-60761-322-0_19

6 Pei, Z. *et al.* Mouse very long-chain Acyl-CoA synthetase 3/fatty acid transport protein 3 catalyzes fatty acid activation but not fatty acid transport in MA-10 cells. *J Biol Chem* **279**, 54454-54462 (2004). https://doi.org:10.1074/jbc.M410091200

7 Schaffer, J. E. Fatty acid transport: the roads taken. *Am J Physiol Endocrinol Metab* **282**, E239-246 (2002). https://doi.org:10.1152/ajpendo.00462.2001

8 Hamilton, J. A. Transport of fatty acids across membranes by the diffusion mechanism. *Prostaglandins Leukot Essent Fatty Acids* **60**, 291-297 (1999). https://doi.org:10.1016/s0952-3278(99)80002-7

9 Veglia, F. *et al.* Fatty acid transport protein 2 reprograms neutrophils in cancer. *Nature* **569**, 73-78 (2019). https://doi.org:10.1038/s41586-019-1118-2

10 Chen, Y. *et al.* Involvement of FATP2-mediated tubular lipid metabolic reprogramming in renal fibrogenesis. *Cell Death Dis* **11**, 994 (2020). https://doi.org:10.1038/s41419-020-03199-x

11 Klar, J. *et al.* Mutations in the fatty acid transport protein 4 gene cause the ichthyosis prematurity syndrome. *Am J Hum Genet* **85**, 248-253 (2009). https://doi.org:10.1016/j.ajhg.2009.06.021

12 Anderson, C. M. & Stahl, A. SLC27 fatty acid transport proteins. *Mol Aspects Med* **34**, 516-528 (2013). https://doi.org:10.1016/j.mam.2012.07.010

13 Schaffer, J. E. & Lodish, H. F. Expression cloning and characterization of a novel adipocyte long chain fatty acid transport protein. *Cell* **79**, 427-436 (1994). https://doi.org:10.1016/0092-8674(94)90252-6

14 Hirsch, D., Stahl, A. & Lodish, H. F. A family of fatty acid transporters conserved from mycobacterium to man. *Proc Natl Acad Sci U S A* **95**, 8625-8629 (1998). https://doi.org:10.1073/pnas.95.15.8625

15 Krammer, J. *et al.* Overexpression of CD36 and acyl-CoA synthetases FATP2, FATP4 and ACSL1 increases fatty acid uptake in human hepatoma cells. *Int J Med Sci* **8**, 599-614 (2011). https://doi.org:10.7150/ijms.8.599

16 Enooku, K. *et al.* Hepatic FATP5 expression is associated with histological progression and loss of hepatic fat in NAFLD patients. *J Gastroenterol* **55**, 227-243 (2020). https://doi.org:10.1007/s00535-019-01633-2

17 Lager, S. *et al.* Protein expression of fatty acid transporter 2 is polarized to the trophoblast basal plasma membrane and increased in placentas from overweight/obese women. *Placenta* **40**, 60-66 (2016). https://doi.org:10.1016/j.placenta.2016.02.010

18 Khan, S. *et al.* Kidney Proximal Tubule Lipoapoptosis Is Regulated by Fatty Acid Transporter-2 (FATP2). *J Am Soc Nephrol* **29**, 81-91 (2018). https://doi.org:10.1681/ASN.2017030314

19 Falcon, A. *et al.* FATP2 is a hepatic fatty acid transporter and peroxisomal very long-chain acyl-CoA synthetase. *Am J Physiol Endocrinol Metab* **299**, E384-393 (2010). https://doi.org:10.1152/ajpendo.00226.2010

20 Pohl, J., Ring, A., Korkmaz, U., Ehehalt, R. & Stremmel, W. FAT/CD36-mediated long-chain fatty acid uptake in adipocytes requires plasma membrane rafts. *Mol Biol Cell* **16**, 24-31 (2005). https://doi.org:10.1091/mbc.e04-07-0616

21 Hao, J. W. *et al.* CD36 facilitates fatty acid uptake by dynamic palmitoylation-regulated endocytosis. *Nat Commun* **11**, 4765 (2020). https://doi.org:10.1038/s41467-020-18565-8

22 Abumrad, N. A., el-Maghrabi, M. R., Amri, E. Z., Lopez, E. & Grimaldi, P. A. Cloning of a rat adipocyte membrane protein implicated in binding or transport of long-chain fatty acids that is induced during preadipocyte differentiation. Homology with human CD36. *J Biol Chem* **268**, 17665-17668 (1993).

23 Jia, Z., Moulson, C. L., Pei, Z., Miner, J. H. & Watkins, P. A. Fatty acid transport protein 4 is the principal very long chain fatty acyl-CoA synthetase in skin fibroblasts. *J Biol Chem* **282**, 20573-20583 (2007). https://doi.org:10.1074/jbc.M700568200

24 Xu, N. *et al.* The FATP1-DGAT2 complex facilitates lipid droplet expansion at the ER-lipid droplet interface. *J Cell Biol* **198**, 895-911 (2012). https://doi.org:10.1083/jcb.201201139

25 Milger, K. *et al.* Cellular uptake of fatty acids driven by the ER-localized acyl-CoA synthetase FATP4. *J Cell Sci* **119**, 4678-4688 (2006). https://doi.org:10.1242/jcs.03280

26 Rönfeldt, S. *et al.* Membrane contacts between caveolae and the endoplasmic reticulum regulate uptake and metabolic trapping of long-chain fatty acids. *bioRxiv*, 2025.2012.2022.695939 (2025). https://doi.org:10.64898/2025.12.22.695939

27 Sandoval, A., Chokshi, A., Jesch, E. D., Black, P. N. & Dirusso, C. C. Identification and characterization of small compound inhibitors of human FATP2. *Biochem Pharmacol* **79**, 990-999 (2010). https://doi.org:10.1016/j.bcp.2009.11.008

28 Dubikovskaya, E., Chudnovskiy, R., Karateev, G., Park, H. M. & Stahl, A. Measurement of long-chain fatty acid uptake into adipocytes. *Methods Enzymol* **538**, 107-134 (2014). https://doi.org:10.1016/B978-0-12-800280-3.00007-4

29 Elegheert, J. *et al.* Lentiviral transduction of mammalian cells for fast, scalable and high-level production of soluble and membrane proteins. *Nat Protoc* **13**, 2991-3017 (2018). https://doi.org:10.1038/s41596-018-0075-9

30 Strzelecka, D., Chmielinski, S., Bednarek, S., Jemielity, J. & Kowalska, J. Analysis of mononucleotides by tandem mass spectrometry: investigation of fragmentation pathways for phosphate- and ribose-modified nucleotide analogues. *Sci Rep* **7**, 8931 (2017). https://doi.org:10.1038/s41598-017-09416-6

31 Schmelz, S. & Naismith, J. H. Adenylate-forming enzymes. *Curr Opin Struct Biol* **19**, 666-671 (2009). https://doi.org:10.1016/j.sbi.2009.09.004

32 Gulick, A. M. Conformational dynamics in the Acyl-CoA synthetases, adenylation domains of non-ribosomal peptide synthetases, and firefly luciferase. *ACS Chem Biol* **4**, 811-827 (2009). https://doi.org:10.1021/cb900156h

33 Wu, D. *et al.* Native MS-guided lipidomics to define endogenous lipid microenvironments of eukaryotic receptors and transporters. *Nat Protoc* **20**, 1-25 (2025). https://doi.org:10.1038/s41596-024-01037-4

34 Melton, E. M., Cerny, R. L., Watkins, P. A., DiRusso, C. C. & Black, P. N. Human fatty acid transport protein 2a/very long chain acyl-CoA synthetase 1 (FATP2a/Acsvl1) has a

preference in mediating the channeling of exogenous n-3 fatty acids into phosphatidylinositol. *J Biol Chem* **286**, 30670-30679 (2011). https://doi.org:10.1074/jbc.M111.226316

35 Heinig, M. & Frishman, D. STRIDE: a web server for secondary structure assignment from known atomic coordinates of proteins. *Nucleic Acids Res* **32**, W500-502 (2004). https://doi.org:10.1093/nar/gkh429

36 Lomize, A. L., Todd, S. C. & Pogozheva, I. D. Spatial arrangement of proteins in planar and curved membranes by PPM 3.0. *Protein Sci* **31**, 209-220 (2022). https://doi.org:10.1002/pro.4219

37 Chong, C. P. *et al.* Bile acid-CoA ligase deficiency--a new inborn error of bile acid metabolism. *J Inherit Metab Dis* **35**, 521-530 (2012). https://doi.org:10.1007/s10545-011-9416-3

38 Kumar, M. *et al.* Definition of fatty acid transport protein-2 (FATP2) structure facilitates identification of small molecule inhibitors for the treatment of diabetic complications. *Int J Biol Macromol* **244**, 125328 (2023). https://doi.org:10.1016/j.ijbiomac.2023.125328

39 Lee, M. C. *et al.* Sar1p N-terminal helix initiates membrane curvature and completes the fission of a COPII vesicle. *Cell* **122**, 605-617 (2005). https://doi.org:10.1016/j.cell.2005.07.025

40 McMahon, H. T. & Gallop, J. L. Membrane curvature and mechanisms of dynamic cell membrane remodelling. *Nature* **438**, 590-596 (2005). https://doi.org:10.1038/nature04396

41 Drin, G. & Antonny, B. Amphipathic helices and membrane curvature. *FEBS Lett* **584**, 1840-1847 (2010). https://doi.org:10.1016/j.febslet.2009.10.022

42 Ford, M. G. *et al.* Curvature of clathrin-coated pits driven by epsin. *Nature* **419**, 361-366 (2002). https://doi.org:10.1038/nature01020

43 Itoh, T. *et al.* Role of the ENTH domain in phosphatidylinositol-4,5-bisphosphate binding and endocytosis. *Science* **291**, 1047-1051 (2001). https://doi.org:10.1126/science.291.5506.1047

44 Boucrot, E. *et al.* Membrane fission is promoted by insertion of amphipathic helices and is restricted by crescent BAR domains. *Cell* **149**, 124-136 (2012). https://doi.org:10.1016/j.cell.2012.01.047

45 Antonny, B. Mechanisms of membrane curvature sensing. *Annu Rev Biochem* **80**, 101-123 (2011). https://doi.org:10.1146/annurev-biochem-052809-155121

46 McMahon, H. T. & Boucrot, E. Membrane curvature at a glance. *J Cell Sci* **128**, 1065-1070 (2015). https://doi.org:10.1242/jcs.114454

47 Bhaskara, R. M. *et al.* Curvature induction and membrane remodeling by FAM134B reticulon homology domain assist selective ER-phagy. *Nat Commun* **10**, 2370 (2019). https://doi.org:10.1038/s41467-019-10345-3

48 Wang, N. *et al.* Mechanism of membrane-curvature generation by ER-tubule shaping proteins. *Nat Commun* **12**, 568 (2021). https://doi.org:10.1038/s41467-020-20625-y

49 Drin, G. *et al.* A general amphipathic alpha-helical motif for sensing membrane curvature. *Nat Struct Mol Biol* **14**, 138-146 (2007). https://doi.org:10.1038/nsmb1194

50 Hatzakis, N. S. *et al.* How curved membranes recruit amphipathic helices and protein anchoring motifs. *Nat Chem Biol* **5**, 835-841 (2009). https://doi.org:10.1038/nchembio.213

51 Saheki, Y. & De Camilli, P. The Extended-Synaptotagmins. *Biochim Biophys Acta Mol Cell Res* **1864**, 1490-1493 (2017). https://doi.org:10.1016/j.bbamcr.2017.03.013

52 Bezawork-Geleta, A. *et al.* Proximity proteomics reveals a mechanism of fatty acid transfer at lipid droplet-mitochondria- endoplasmic reticulum contact sites. *Nat Commun* **16**, 2135 (2025). https://doi.org:10.1038/s41467-025-57405-5

53 Go, C. D. *et al.* A proximity-dependent biotinylation map of a human cell. *Nature* **595**, 120-124 (2021). https://doi.org:10.1038/s41586-021-03592-2

54 Beck, R. *et al.* Membrane curvature induced by Arf1-GTP is essential for vesicle formation. *Proc Natl Acad Sci U S A* **105**, 11731-11736 (2008). https://doi.org:10.1073/pnas.0805182105

55 Ishida, M. & Bonifacino, J. S. ARFRP1 functions upstream of ARL1 and ARL5 to coordinate recruitment of distinct tethering factors to the trans-Golgi network. *J Cell Biol* **218**, 3681-3696 (2019). https://doi.org:10.1083/jcb.201905097

56 Faust, J. E. *et al.* The Atlastin C-terminal tail is an amphipathic helix that perturbs the bilayer structure during endoplasmic reticulum homotypic fusion. *J Biol Chem* **290**, 4772-4783 (2015). https://doi.org:10.1074/jbc.M114.601823

57 Lee, C. & Goldberg, J. Structure of coatomer cage proteins and the relationship among COPI, COPII, and clathrin vesicle coats. *Cell* **142**, 123-132 (2010). https://doi.org:10.1016/j.cell.2010.05.030

58 Stagg, S. M. *et al.* Structure of the Sec13/31 COPII coat cage. *Nature* **439**, 234-238 (2006). https://doi.org:10.1038/nature04339

59 Stagg, S. M. *et al.* Structural basis for cargo regulation of COPII coat assembly. *Cell* **134**, 474-484 (2008). https://doi.org:10.1016/j.cell.2008.06.024

60 Giordano, F. *et al.* PI(4,5)P(2)-dependent and Ca(2+)-regulated ER-PM interactions mediated by the extended synaptotagmins. *Cell* **153**, 1494-1509 (2013). https://doi.org:10.1016/j.cell.2013.05.026

61 Singh, N. *et al.* Redefining the specificity of phosphoinositide-binding by human PH domain-containing proteins. *Nat Commun* **12**, 4339 (2021). https://doi.org:10.1038/s41467-021-24639-y

62 Harlan, J. E., Hajduk, P. J., Yoon, H. S. & Fesik, S. W. Pleckstrin homology domains bind to phosphatidylinositol-4,5-bisphosphate. *Nature* **371**, 168-170 (1994). https://doi.org:10.1038/371168a0

63 Tang, H. *et al.* The solute carrier SPNS2 recruits PI(4,5)P(2) to synergistically regulate transport of sphingosine-1-phosphate. *Mol Cell* **83**, 2739-2752 e2735 (2023). https://doi.org:10.1016/j.molcel.2023.06.033

64 Kunkl, M. *et al.* ISA-2011B, a Phosphatidylinositol 4-Phosphate 5-Kinase alpha Inhibitor, Impairs CD28-Dependent Costimulatory and Pro-inflammatory Signals in Human T Lymphocytes. *Front Immunol* **8**, 502 (2017). https://doi.org:10.3389/fimmu.2017.00502

65 Wright, B. D. *et al.* The lipid kinase PIP5K1C regulates pain signaling and sensitization. *Neuron* **82**, 836-847 (2014). https://doi.org:10.1016/j.neuron.2014.04.006

66 Hisanaga, Y. *et al.* Structural basis of the substrate-specific two-step catalysis of long chain fatty acyl-CoA synthetase dimer. *J Biol Chem* **279**, 31717-31726 (2004). https://doi.org:10.1074/jbc.M400100200

67 Vanni, S. *et al.* Amphipathic lipid packing sensor motifs: probing bilayer defects with hydrophobic residues. *Biophys J* **104**, 575-584 (2013). https://doi.org:10.1016/j.bpj.2012.11.3837

68 Rogers, J. R., Espinoza Garcia, G. & Geissler, P. L. Membrane hydrophobicity determines the activation free energy of passive lipid transport. *Biophys J* **120**, 3718-3731 (2021). https://doi.org:10.1016/j.bpj.2021.07.016

69 Voeltz, G. K., Sawyer, E. M., Hajnoczky, G. & Prinz, W. A. Making the connection: How membrane contact sites have changed our view of organelle biology. *Cell* **187**, 257-270 (2024). https://doi.org:10.1016/j.cell.2023.11.040

70 Abramson, J. *et al.* Accurate structure prediction of biomolecular interactions with AlphaFold 3. *Nature* **630**, 493-500 (2024). https://doi.org:10.1038/s41586-024-07487-w

71 Gautier, R., Douguet, D., Antonny, B. & Drin, G. HELIQUEST: a web server to screen sequences with specific alpha-helical properties. *Bioinformatics* **24**, 2101-2102 (2008). https://doi.org:10.1093/bioinformatics/btn392

72 Liu, H. & Naismith, J. H. An efficient one-step site-directed deletion, insertion, single and multiple-site plasmid mutagenesis protocol. *BMC Biotechnol* **8**, 91 (2008). https://doi.org:10.1186/1472-6750-8-91

73 Matsuda, A., Schermelleh, L., Hirano, Y., Haraguchi, T. & Hiraoka, Y. Accurate and fiducial-marker-free correction for three-dimensional chromatic shift in biological fluorescence microscopy. *Sci Rep* **8**, 7583 (2018). https://doi.org:10.1038/s41598-018-25922-7

74 Marty, M. T. *et al.* Bayesian deconvolution of mass and ion mobility spectra: from binary interactions to polydisperse ensembles. *Anal Chem* **87**, 4370-4376 (2015). https://doi.org:10.1021/acs.analchem.5b00140

75 Punjani, A., Rubinstein, J. L., Fleet, D. J. & Brubaker, M. A. cryoSPARC: algorithms for rapid unsupervised cryo-EM structure determination. *Nat Methods* **14**, 290-296 (2017). https://doi.org:10.1038/nmeth.4169

76 Williams, C. J. *et al.* MolProbity: More and better reference data for improved all-atom structure validation. *Protein Sci* **27**, 293-315 (2018). https://doi.org:10.1002/pro.3330

77 Emsley, P., Lohkamp, B., Scott, W. G. & Cowtan, K. Features and development of Coot. *Acta Crystallogr D Biol Crystallogr* **66**, 486-501 (2010). https://doi.org:10.1107/S0907444910007493

78 Afonine, P. V. *et al.* Towards automated crystallographic structure refinement with phenix.refine. *Acta Crystallogr D Biol Crystallogr* **68**, 352-367 (2012). https://doi.org:10.1107/S0907444912001308

79 Pettersen, E. F. *et al.* UCSF ChimeraX: Structure visualization for researchers, educators, and developers. *Protein Sci* **30**, 70-82 (2021). https://doi.org:10.1002/pro.3943

80 Konagurthu, A. S., Whisstock, J. C., Stuckey, P. J. & Lesk, A. M. MUSTANG: a multiple structural alignment algorithm. *Proteins* **64**, 559-574 (2006). https://doi.org:10.1002/prot.20921

81 Jumper, J. *et al.* Highly accurate protein structure prediction with AlphaFold. *Nature* **596**, 583-589 (2021). https://doi.org:10.1038/s41586-021-03819-2

82 Fleming, J. *et al.* AlphaFold Protein Structure Database and 3D-Beacons: New Data and Capabilities. *J Mol Biol* **437**, 168967 (2025). https://doi.org:10.1016/j.jmb.2025.168967

83 Osorio, D., Rondon-Villarreal, P., Torres, R. Peptides: A package for data mining of antimicrobial peptides. *The R Journal* **7**, 4-14 (2015).

84 Eisenberg, D., Weiss, R. M. & Terwilliger, T. C. The hydrophobic moment detects periodicity in protein hydrophobicity. *Proc Natl Acad Sci U S A* **81**, 140-144 (1984). https://doi.org:10.1073/pnas.81.1.140

85 Jo, S., Kim, T., Iyer, V. G. & Im, W. CHARMM-GUI: a web-based graphical user interface for CHARMM. *J Comput Chem* **29**, 1859-1865 (2008). https://doi.org:10.1002/jcc.20945

86 Lee, J. *et al.* CHARMM-GUI Input Generator for NAMD, GROMACS, AMBER, OpenMM, and CHARMM/OpenMM Simulations Using the CHARMM36 Additive Force Field. *J Chem Theory Comput* **12**, 405-413 (2016). https://doi.org:10.1021/acs.jctc.5b00935

87 Best, R. B. *et al.* Optimization of the additive CHARMM all-atom protein force field targeting improved sampling of the backbone phi, psi and side-chain chi(1) and chi(2) dihedral angles. *J Chem Theory Comput* **8**, 3257-3273 (2012). https://doi.org:10.1021/ct300400x

88 Jorgensen, W. L., Chandrasekhar, J., Madura, J. D., Impey, R. W. & Klein, M. L. Comparison of simple potential functions for simulating liquid water. *The Journal of Chemical Physics* **79**, 926-935 (1983). https://doi.org:10.1063/1.445869

89 Price, D. J. & Brooks, C. L., 3rd. A modified TIP3P water potential for simulation with Ewald summation. *J Chem Phys* **121**, 10096-10103 (2004). https://doi.org:10.1063/1.1808117

90 Kräutler, V., Van Gunsteren, W. F. & Hünenberger, P. H. A fast SHAKE algorithm to solve distance constraint equations for small molecules in molecular dynamics simulations. *Journal of computational chemistry* **22**, 501-508 (2001).

91 Van Der Spoel, D. *et al.* GROMACS: fast, flexible, and free. *J Comput Chem* **26**, 1701-1718 (2005). https://doi.org:10.1002/jcc.20291

92 Abraham, M. J. *et al.* GROMACS: High performance molecular simulations through multi-level parallelism from laptops to supercomputers. *SoftwareX* **1**, 19-25 (2015).

93 Essmann, U. *et al.* A smooth particle mesh Ewald method. *The Journal of chemical physics* **103**, 8577-8593 (1995).

94 Hess, B., Bekker, H., Berendsen, H. J. & Fraaije, J. G. LINCS: A linear constraint solver for molecular simulations. *Journal of computational chemistry* **18**, 1463-1472 (1997).

95 Hess, B. P-LINCS: A Parallel Linear Constraint Solver for Molecular Simulation. *J Chem Theory Comput* **4**, 116-122 (2008). https://doi.org:10.1021/ct700200b

96 Bussi, G., Donadio, D. & Parrinello, M. Canonical sampling through velocity rescaling. *The Journal of chemical physics* **126** (2007).

97 Bernetti, M. & Bussi, G. Pressure control using stochastic cell rescaling. *The Journal of Chemical Physics* **153** (2020).

98 Humphrey, W., Dalke, A. & Schulten, K. VMD: visual molecular dynamics. *Journal of molecular graphics* **14**, 33-38 (1996).

99 Tomasello, G., Armenia, I. & Molla, G. The Protein Imager: a full-featured online molecular viewer interface with server-side HQ-rendering capabilities. *Bioinformatics* **36**, 2909-2911 (2020). https://doi.org:10.1093/bioinformatics/btaa009

100 Gowers, R. J. *et al.* MDAnalysis: a Python package for the rapid analysis of molecular dynamics simulations. Report No. 2575-9752, (Los Alamos National Laboratory (LANL), Los Alamos, NM (United States), 2019).

101 Michaud‐Agrawal, N., Denning, E. J., Woolf, T. B. & Beckstein, O. MDAnalysis: a toolkit for the analysis of molecular dynamics simulations. *Journal of computational chemistry* **32**, 2319-2327 (2011).

102 Tsugawa, H. *et al.* A lipidome atlas in MS-DIAL 4. *Nat Biotechnol* **38**, 1159-1163 (2020). https://doi.org:10.1038/s41587-020-0531-2

103 Yu, F. *et al.* Analysis of DIA proteomics data using MSFragger-DIA and FragPipe computational platform. *Nat Commun* **14**, 4154 (2023). https://doi.org:10.1038/s41467-023-39869-5

104 Demichev, V., Messner, C. B., Vernardis, S. I., Lilley, K. S. & Ralser, M. DIA-NN: neural networks and interference correction enable deep proteome coverage in high throughput. *Nat Methods* **17**, 41-44 (2020). https://doi.org:10.1038/s41592-019-0638-x

Supplementary Files

This is a list of supplementary files associated with this preprint. Click to download.

- cvrFATP2SupplementaryHS260216.pdf